NAVAL POSTGRADUATE SCHOOL

MONTEREY, CALIFORNIA

THESIS

METAMATERIAL FOR RADAR FREQUENCIES

by

Szu Hau Tan

September 2012

Thesis Advisor: David C. Jenn
Second Reader: James Calusdian

Approved for public release; distribution is unlimited

THIS PAGE INTENTIONALLY LEFT BLANK

REPORT DOCUMENTATION PAGE			Form Approved OMB No. 0704-0188
Public reporting burden for this collection of information is estimated to average 1 hour per response, including the time for reviewing instruction, searching existing data sources, gathering and maintaining the data needed, and completing and reviewing the collection of information. Send comments regarding this burden estimate or any other aspect of this collection of information, including suggestions for reducing this burden, to Washington headquarters Services, Directorate for Information Operations and Reports, 1215 Jefferson Davis Highway, Suite 1204, Arlington, VA 22202-4302, and to the Office of Management and Budget, Paperwork Reduction Project (0704-0188) Washington DC 20503.			
1. AGENCY USE ONLY ***(Leave blank)***	**2. REPORT DATE** September 2012	**3. REPORT TYPE AND DATES COVERED** Master's Thesis	
4. TITLE AND SUBTITLE Metamaterial for Radar Frequencies		**5. FUNDING NUMBERS**	
6. AUTHOR(S) Szu Hau Tan			
7. PERFORMING ORGANIZATION NAME(S) AND ADDRESS(ES) Naval Postgraduate School Monterey, CA 93943-5000		**8. PERFORMING ORGANIZATION REPORT NUMBER**	
9. SPONSORING /MONITORING AGENCY NAME(S) AND ADDRESS(ES) N/A		**10. SPONSORING/MONITORING AGENCY REPORT NUMBER**	
11. SUPPLEMENTARY NOTES The views expressed in this thesis are those of the author and do not reflect the official policy or position of the Department of Defense or the U.S. Government.			
12a. DISTRIBUTION / AVAILABILITY STATEMENT Approved for public release; distribution is unlimited		**12b. DISTRIBUTION CODE** A	

13. ABSTRACT (maximum 200 words)

The objective of this thesis is to investigate a new design of periodic metamaterial (MTM) structure for radar cross-section (RCS) reduction application on aircraft and ships. MTMs are man-made materials, not found in nature, that exhibit unusual properties in the radio-, electromagnetic-, and optical-wave bands. The cells of these periodic MTM structures must be much smaller than the wavelength of the frequency of interest. In a MTM, the structure and dimensions of the design at the frequency of interest can produce negative values of permeability and/or permittivity, which define the electrical properties of the MTM. This study looks at various designs of absorbing layers presented in technical papers and verifies the results in simulations. Modifications are done to the existing designs to achieve good absorption level at the radar-frequency band of interest. Modeling and simulation are done in Microwave Studio by Computer Simulation Technology (CST). The S-parameters S_{11} (reflection coefficient) and S_{12} (transmission coefficient) are used to investigate the performance of the MTM as a radar-frequency absorber.

14. SUBJECT TERMS Metamaterials, Negative Index, Radar Cross Section, Permittivity and Permeability.			**15. NUMBER OF PAGES** 82
			16. PRICE CODE
17. SECURITY CLASSIFICATION REPORT Unclassified	**18. SECURITY CLASSIFICATION OF THIS PAGE** Unclassified	**19. SECURITY CLASSIFICATION OF ABSTRACT** Unclassified	**20. LIMITATION OF ABSTRACT** UU

NSN 7540-01-280-5500 Standard Form 298 (Rev. 2-89)
Prescribed by ANSI Std. 239-18

THIS PAGE INTENTIONALLY LEFT BLANK

Approved for public release; distribution is unlimited

METAMATERIAL FOR RADAR FREQUENCIES

Szu Hau Tan
Civilian, Singapore Technologies Aerospace Ltd.
B.S., University of Glasgow, 1998.

Submitted in partial fulfillment of the
requirements for the degree of

MASTER OF SCIENCE IN ELECTRICAL ENGINEERING

from the

NAVAL POSTGRADUATE SCHOOL
September 2012

Author: Szu Hau Tan

Approved by: David C. Jenn
Thesis Advisor

James Calusdian
Second Reader

R. Clark Robertson
Chair, Department of Electrical and Computer Engineering

THIS PAGE INTENTIONALLY LEFT BLANK

ABSTRACT

The objective of this thesis is to investigate a new design of periodic metamaterial (MTM) structure for radar cross-section (RCS) reduction application on aircraft and ships. MTMs are man-made materials, not found in nature, that exhibit unusual properties in the radio-, electromagnetic-, and optical-wave bands. The cells of these periodic MTM structures must be much smaller than the wavelength of the frequency of interest. In a MTM, the structure and dimensions of the design at the frequency of interest can produce negative values of permeability and/or permittivity, which define the electrical properties of the MTM. This study looks at various designs of absorbing layers presented in technical papers and verifies the results in simulations. Modifications are done to the existing designs to achieve good absorption level at the radar-frequency band of interest. Modeling and simulation are done in Microwave Studio by Computer Simulation Technology (CST). The S-parameters S_{11} (reflection coefficient) and S_{12} (transmission coefficient) are used to investigate the performance of the MTM as a radar-frequency absorber.

THIS PAGE INTENTIONALLY LEFT BLANK

TABLE OF CONTENTS

LIST OF FIGURES

LIST OF TABLES

THIS PAGE INTENTIONALLY LEFT BLANK

LIST OF ACRONYMS AND ABBREVIATIONS

ADS	Advance Design System
CPR	Coplanar Ring
CST	Computer Simulation Technology
DNG	Double Negative Material
DPS	Double Positive Material
EM	Electromagnetic
ERR	Electric Ring Resonator
FIT	Finite Integration Technique
LH	Left-Handed
MTM	Metamaterial
MWS	Microwave Studio by CST
NIM	Negative Index Material
OTH	Over-The-Horizon
PCB	Printed Circuit Board
RAM	Radar Absorbing Material
RCS	Radar Cross Section
SNR	Signal-to-Noise Ratio
SNG	Single-Negative
SRR	Split Ring Resonator

THIS PAGE INTENTIONALLY LEFT BLANK

EXECUTIVE SUMMARY

Since the invention of radar, attempts to counter radar detection have been investigated. There are four basic ways to do this: (a) shaping of the platform, (b) application of radar-absorbing material to the platform, (c) disrupting the radar's receiver by electronic jamming and (d) flying under the radar. Option (a) can only be realized at the platform's design stage. Existing platforms without shaping incorporated into the design can only use options (b), (c) and (d). The problem with option (b) is the weight involved. Radar-absorbing material (RAM) usually consists of iron powder as inclusions in a primary binding matrix like polyurethane. Additional weight on an aircraft is a big issue because it compromises the amount and type of armaments that can be carried. Option (c) also reduces the amount of weaponry an aircraft can carry. Option (d) is not always feasible, as it may be geographically impossible and only avoids ground radars at best.

In this thesis, the objective of the study was to design a new metamaterial (MTM) for application to platform surfaces. The MTM will be a radar absorber to reduce the platform's radar cross-section (RCS) signature, thereby making the platform less detectable at long range by C- and X-band radars. The MTM will be lighter than conventional RAM coatings since it contains no iron inclusions and can be made much thinner.

Materials are electrically defined by their permittivity and permeability. Most naturally occurring material possesses positive permittivity and permeability, but a MTM's permittivity and permeability can have either one or both negative. MTMs are man-made materials that possess interesting properties like negative index of refraction that bend electromagnetic (EM) waves to the same side of the normal as the incident wave when the EM wave travels through them, reversing Snell's law of refraction.

Much research on MTM is based on the split-ring resonator, developed by Pendry et al. in 1999 [1]. The objective of this study was to find a new MTM design, departing from the traditional approach. This research is based on a design presented in [2], which describes a MTM with almost complete absorption. The design was replicated in Microwave Studio (MWS) by Computer Simulation Technology (CST). The results

obtained in the simulations were in good agreement with the reported results with regard to the frequency dependence of the absorption and its level.

Modifications to the design in [2] were made to adjust the frequency and improve the absorption. The original design is a free standing surface; that is, it operates with free space on both sides. The configuration was modified so that it could be placed on a conducting surface. Six new designs, made up of basic coplanar rings and cut wires, were tested, but only two gave promising results. One of the promising modifications, Design (c), depicted in Figure 1, was tested extensively, and the parameters in the unit cell were optimized for better performance. The parameters of the unit cell of Design (c) are shown in Table 1. Detailed simulation settings are provided in Chapter III. The u, v and w axes in Figure 1 refer to the working coordinate system and correspond to the x, y and z axes, respectively, in the global coordinate system.

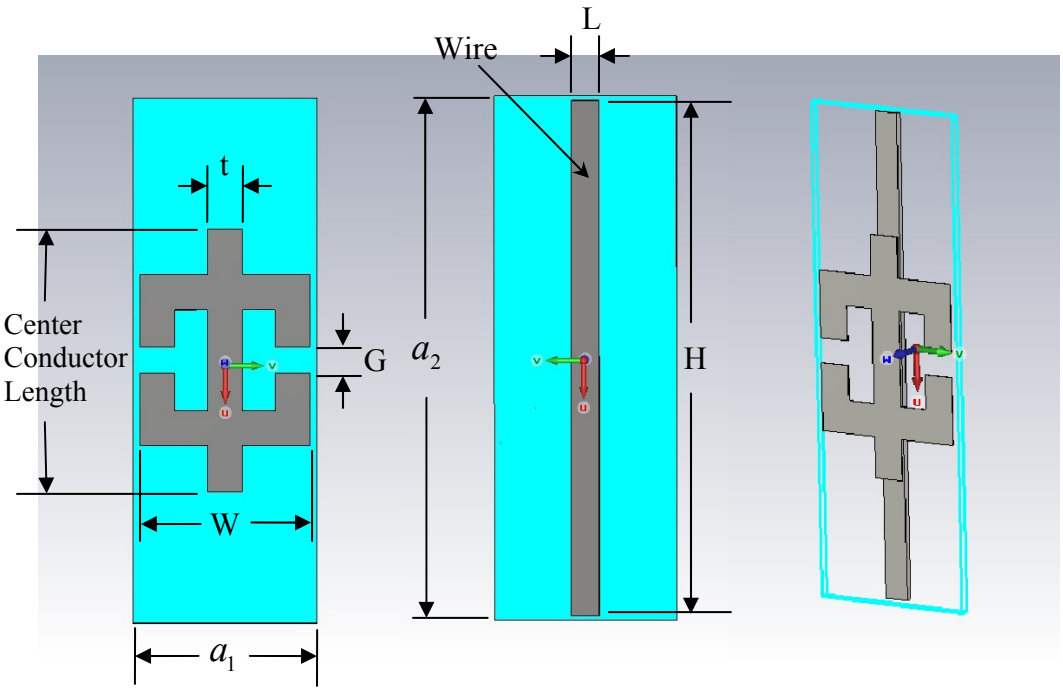

Figure 1. Unit-cell design for Design (c)

During the course of optimization of Design (c) in simulations, it was found that certain parameters are able to shift the frequency of absorption around the selected frequency band. The first of these parameters is the width of the cell *W*, because it is

proportional to the wavelength and determines in which frequency band the absorption lies. Other parameters, like width of wire, thickness of wire, separation distance between unit cells, conductor width, and length of center conductor can also affect the absorption frequency, but these parameters are used to fine tune the frequency and the absorption level within the frequency band.

Table 1. Parameters used in Design (c) simulations.

Parameter	**Dimension (mm)**
a_1	4.2
a_2	12.0
W	3.9
G	0.606
t	0.8
L	0.64
H	11.8
Center Conductor Length	6.0
Conductor thickness	0.017
Substrate thickness	0.2
Wire thickness	0.15
Separation distance between unit cell	1.7
Number of unit cell layers	3 pieces

The two-port simulation result of Design (c) is shown in Figure 2. The result was comparable to the result reported in [2]. A reflection coefficient (scattering parameter S_{22}) of 0.0418 (–27.57 dB) and transmission coefficient (scattering parameter S_{12}) of

0.0637 (–23.91 dB) were achieved. The simulated result of Design (c) on a conducting surface was shown in Figure 3. It achieved a reflection coefficient of 0.02053 (–33.75 dB).

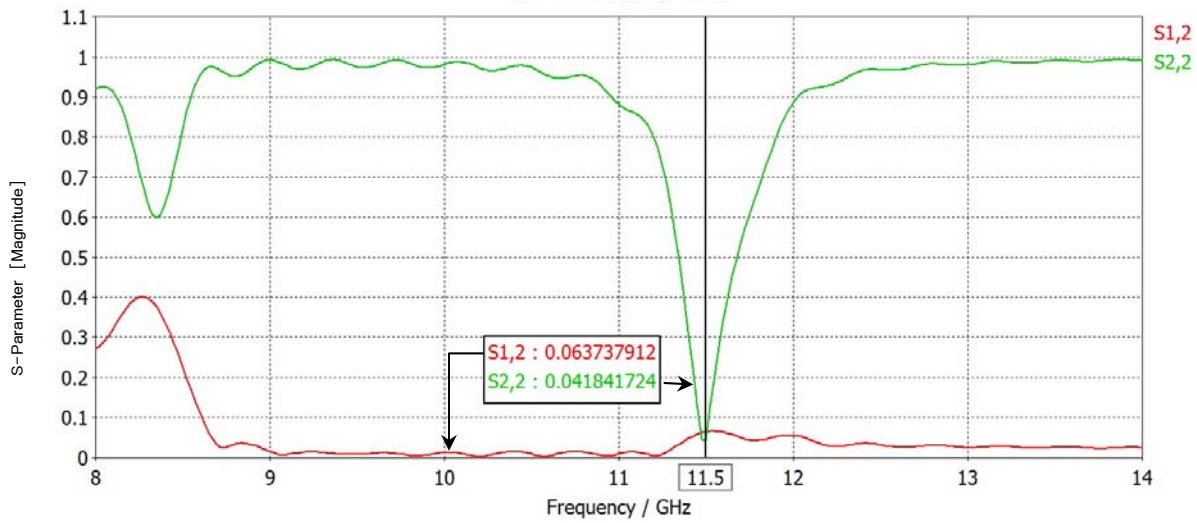

Figure 2. The two port simulation result of Design (c). Reflection coefficient of 0.0418 (–27.57 dB) and transmission coefficient of 0.0637 (–23.91 dB).

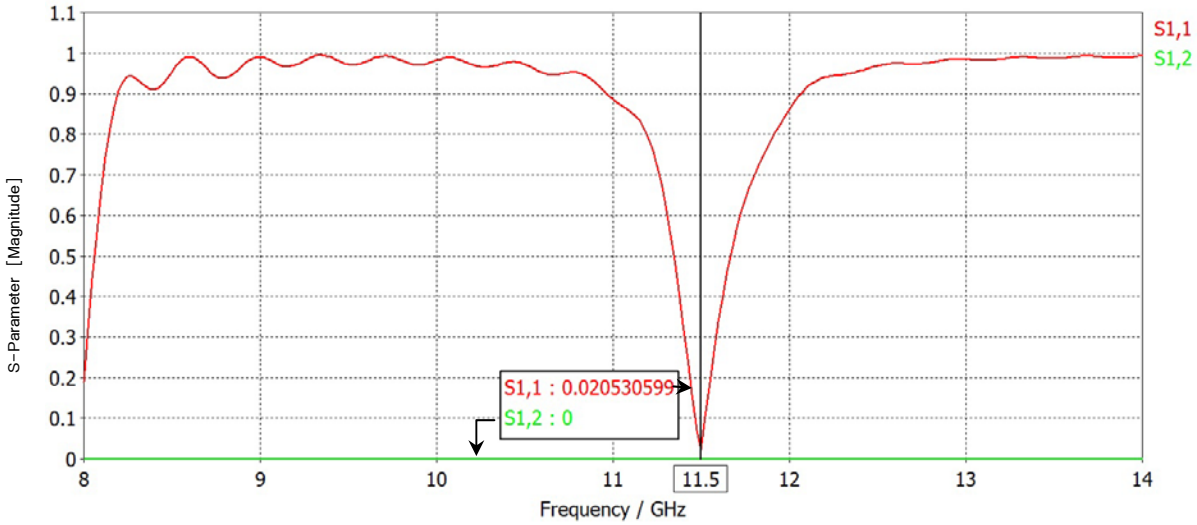

Figure 3. The result of Design (c) on a conducting surface. Reflection coefficient of 0.0205 (–33.75 dB).

The objective of this study was to find a new MTM design for X-band radar frequencies that could be applied to a metallic surface. Hence, the design, modeling and simulation of a new MTM, which was a modification of the design in [2] is described in this thesis. A detailed description of Design (c) was given, with dimensions as in Table 1.

During the course of this study, new questions were raised that need to be addressed in future research. It has been shown with Design (e) that better performance in some areas is possible. The recommended areas for future investigation are:

1. Simulation with a low density spacer between the dielectric layers.
2. Design a dual-polarization MTM.
3. Improve the bandwidth.
4. Derive an equivalent circuit for Design (c).
5. Extract the effective ε and μ of the structure from simulated scattering parameters S_{11} and S_{12}.
6. Extend the design to be effective for other than normal incidence.

EXECUTIVE SUMMARY REFERENCES

[1] J. B. Pendry, A. J. Holden, D. J. Robbins, and W. J. Stewart, "Magnetism from Conductors and Enhanced Nonlinear Phenomena", *IEEE Trans. Microwave Theory Tech.*, vol 47, no.11, pp. 2075-2084, November 1999.

[2] N. I. Landy, S. Sajuyigbe, J. J. Mock, D. R. Smith, and W. J. Padilla, "Perfect Metamaterial Absorber", *Phys. Rev. Letters*, vol. 100, paper 207402, 2008.

ACKNOWLEDGEMENTS

I would like to take this opportunity to thank my company, Singapore Technologies Aerospace Limited, for giving me this wonderful opportunity to further my studies at the Naval Postgraduate School, Monterey, California.

I would also wish to express my utmost gratitude to Professor David C. Jenn of the Naval Postgraduate School for being my thesis advisor and for his patience and guidance in seeing me through the completion of this thesis. I thank Dr. James Calusdian for being my second reader for this thesis and accommodating to my schedule.

Most of all, I cannot sufficiently thank my supportive wife, who came with me to Monterey, for all the things that she has done to allow me to concentrate on my studies and for her good job in taking care of our two wonderful children.

THIS PAGE INTENTIONALLY LEFT BLANK

I. INTRODUCTION

A. BACKGROUND

The principle of radar works by transmitting an electromagnetic (EM) wave and detecting a reflected echo from the target. If there is a target present with sufficient signal-to-noise ratio (SNR), then a detection is declared. Every target has a signature. In the radar world, this signature is known as the radar cross section (RCS). The RCS is the collective scattering from all the contributors on the platform. Military radars are classified into search and surveillance or targeting radars. For over-the-horizon (OTH) surveillance, low frequencies like HF to UHF bands are used (Table 1). These frequencies have long wavelengths which can propagate very long distances. Mid-range surveillance radars use higher frequencies like L or S-band. The C and X-band radars are used for tracking because they offer better down-range and cross-range resolution.

Table 1. Radar-frequency bands and some military applications (From [1]).

Radar Frequency Bands		
Band Designation	**Frequency Range**	**Typical Usage**
VHF	50-330 MHz.	Very long-range surveillance
UHF	300-1,000 MHz.	Very long-range surveillance
L	1-2 GHz.	Long-range surveillance, enroute traffic control
S	2-4 GHz.	Moderate-range surveillance, terminal traffic control, long-range weather
C	4-8 GHz.	Long-range tracking, airborne weather
X	8-12 GHz.	Short-range tracking, missile guidance, mapping, marine radar, airborne intercept
K_u	12-18 GHz.	High resolution mapping, satellite altimetry
K	18-27 GHz.	Little used (H_20 absorption)
K_a	27-40 GHz.	Very high resolution mapping, airport surveillance
mm	40-100+ GHz.	Experimental

The C- and X-bands are the frequency bands of interest in this research because they are used for tracking and short range search radar. If long-range surveillance radar can detect a target, but the tracking radar cannot track and pinpoint the target, the attacker will not be able to fire the weapon.

One way of reducing the signature of an existing platform is by the use of radar absorbing material (RAM). A major issue with RAM coatings is the weight. These materials consist of iron powder as inclusions in a primary binding matrix like polyurethane. However, to achieve the required absorption, the thickness and weight of conventional material is too large. One possible solution for overcoming the weight and volume issues is to use new engineered metamaterials (MTMs). MTMs are man-made, macroscopic, composite materials that possess properties not found in nature. They are comprised of "cells" with inclusions that take on many forms, such as spheres and rings. If the cells are small compared to wavelength, then the material is effectively homogeneous. These materials are designed and structured to manipulate the propagation of electromagnetic waves that impinge on them. An application for MTMs that many researchers are looking into is platform cloaking, rendering a platform invisible and undetectable by radar [2–4].

If a platform is covered with MTMs designed to work in the radar's frequency range, the EM wave from the radar will either be directed around the platform and continue its path (cloaking) or be completely absorbed by the MTM. In the second scenario, the MTM works as a radar-absorbing material. Either way, the RCS of the platform is reduced, as no EM wave is reflected back to the radar. Thus, monostatic radar will not detect the presence of a platform.

Electrically, materials are defined by their permittivity ε and permeability μ, which are complex quantities in the frequency domain:

$$\varepsilon = \varepsilon_o \varepsilon_r = \varepsilon_o (\varepsilon_r' - j\varepsilon_r'') \tag{1.1}$$

$$\mu = \mu_o \mu_r = \mu_o (\mu_r' - j\mu_r'') \tag{1.2}$$

where $\varepsilon_0 = 8.854 \times 10^{-12}$ F/m is the permittivity of free space and $\mu_0 = 4\pi \times 10^{-7}$ H/m is the permeability of free space. Here the $e^{j\omega t}$ time convention is used. The complex index of refraction of the material is:

$$n \equiv \sqrt{\varepsilon_r \mu_r} \,. \tag{1.3}$$

MTMs can have a negative refractive index. For a lossless material ($\varepsilon_r'' = \mu_r'' = 0$),

$$n = \sqrt{\varepsilon_r' \mu_r'} \,. \tag{1.4}$$

If both μ_r' and ε_r' are negative, they are called negative-index materials (NIM), also known as double-negative material (DNG). DNG materials have some unique propagation characteristics, as will be discussed in the next chapter.

Permittivity and permeability are the two parameters that determine an MTM's response to EM waves. Most natural materials have positive relative permittivity and permeability. Some materials have negative permittivity or permeability [5]. At the resonant frequency of a DNG MTM, both permittivity and permeability are negative, as shown in Figure 1, resulting in a negative refractive index. Among the unique EM propagation properties of DNG materials is that the phase fronts propagate in a direction opposite to the power flow given by the Poynting vector. This has led to the designation of DNG material as left-handed (LH) materials.

Permittivity and permeability can be determined by measuring the complex (magnitude and phase) EM wave reflection and transmission coefficients of a material sample. For several reasons, difficulties arise in obtaining permittivity and permeability when the material under test is a MTM. One is that the properties of a MTM are frequency dependent. In measuring the coefficients, a sweep of frequencies is used so that the resonant frequency can be found. Waveguide measurement is preferred, because large samples, which take time and money to fabricate, are not required. In free space there is diffraction around the edges of the test sample and wave interactions with other objects and the environment, which lead to measurement errors.

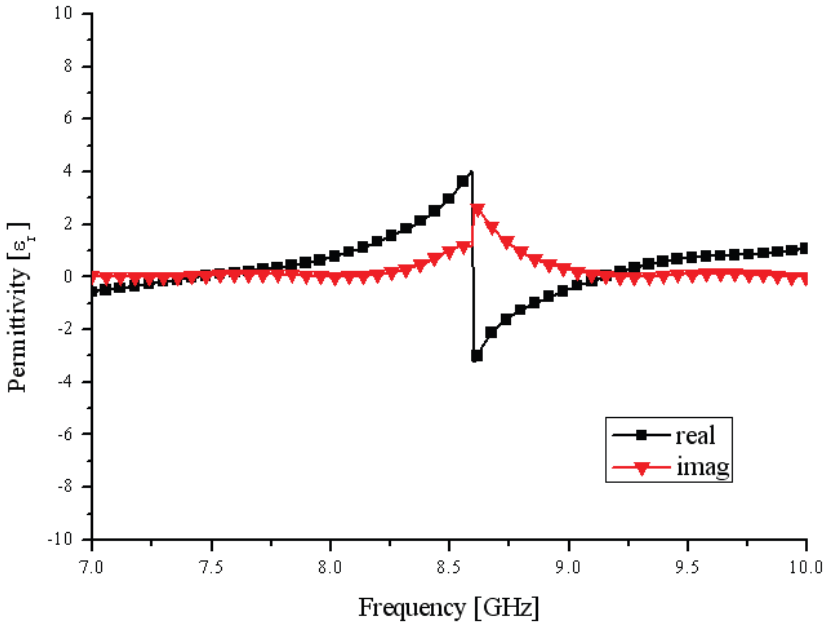

(a)

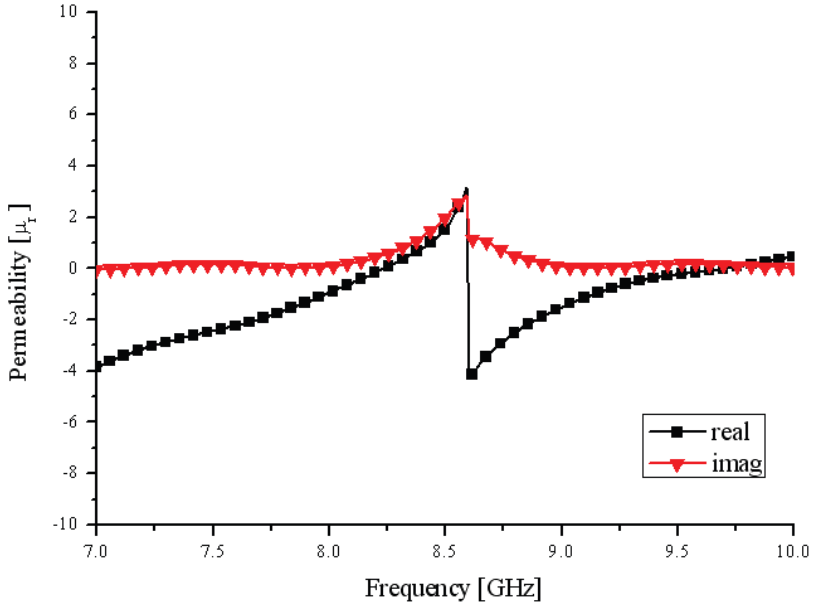

(b)

Figure 1. (a) Example of a material's measured negative permittivity and (b) negative permeability. Notice that both permittivity and permeability are negative at the resonant frequency (From [6]).

When the MTM's inclusion dimensions (cell sizes) are much smaller than the wavelength of the EM wave, the MTM can be homogenized as a medium with effective dielectric and magnetic properties [7]. Although "small" generally refers to much less than the wavelength λ, cell sizes of up to 0.25λ have been used. A "two-dimensionally" isotropic MTM made of coplanar rings and wires is shown in Figure 2.

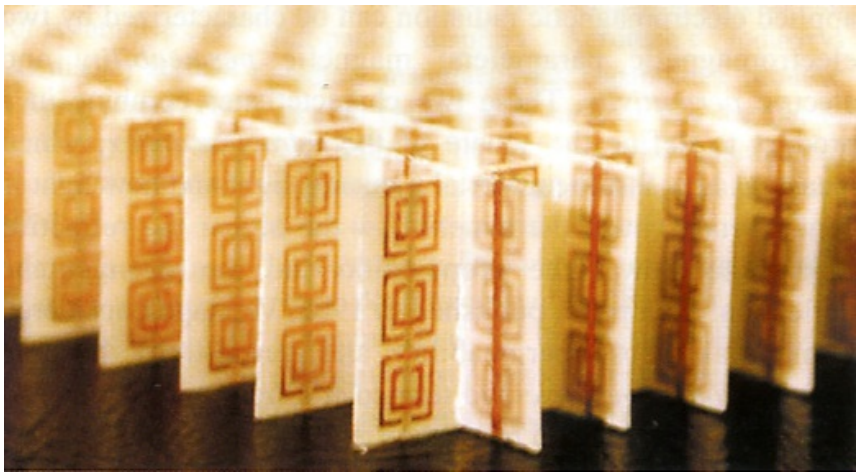

Figure 2. Metamaterial made up of a structure of split-ring resonators and wires. Cell size of each SRR is much smaller than λ (From [11]).

B. LITERATURE REVIEW

1. Historical Background

In 1967, V. G. Veselago investigated theoretically the interaction of a plane wave on a material with negative permittivity and permeability [8]. He believed that such a homogeneous material could be fabricated with a semiconductor. There was no technology to fabricate such a material then, and his work was ignored. It was not until twenty-nine years later that J. B. Pendry revisited V. G. Veselago's theory and published a paper [9] about an artificial metallic construction that exhibited negative relative permittivity ε_r. In 2001, Smith [10] conducted a demonstration that a structure consisting of split-ring resonators (SRR) and wires can represent V. G. Veselago's theory. From then on, interest in MTMs grew, and many papers on applications of MTMs have been published.

Left-handed materials like metal wires and split-ring resonators are intrinsically lossy and narrowband [12]. Another method of achieving LH material with lower loss and wider bandwidth is based on transmission-line theory. The periodic structure consists of unit cells of square metal patches with a via to the ground plane. Metal caps below the metal patches provide the capacitive coupling with adjacent patches, as shown in Figure 3. The via provides inductance to ground.

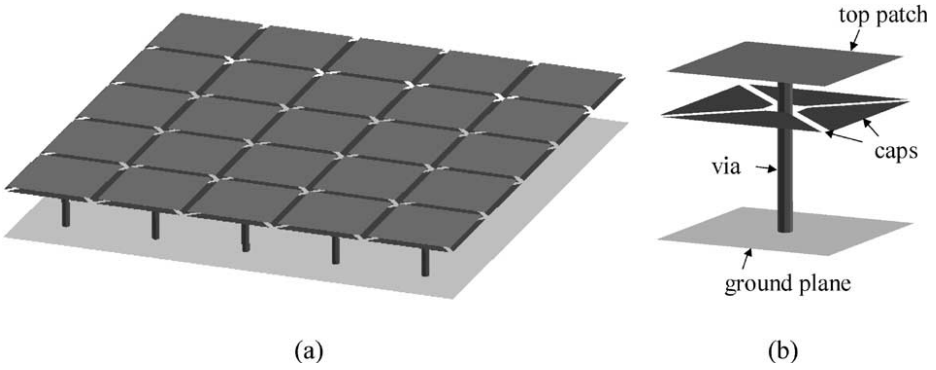

Figure 3. (a) Planar LH distributed periodic structure and its (b) unit cell (From [12]).

The structure presented in [12] shows strong LH properties due to series capacitance provided by an extra layer of metal caps, but the reactance of the cap shifts the operational frequency lower. The structure is isotropic in two dimensions when the operational wavelength is large compared to the size of the unit cell. The structure can be anisotropic if the unit cell is rectangular (rather than square) or if the metal-cap shape is changed to get different capacitance values in different directions. The absolute value of refractive index decreases as frequency increases and become less than one in the fast-wave region where the LH phase velocity is greater than in air.

It is noted in reference [13] that an array of thin metallic wires creates a negative permittivity medium, and an array of SRRs creates the resonant form of effective magnetic permeability. Together they provide LH properties that can be seen only when the EM propagation is in a direction with $\vec{E}$ parallel to the wires and $\vec{H}$ parallel to the ring axis. When the system length is less than ten unit cells, transmission quickly oscillates and decreases exponentially, due to large complex index of refraction.

C. THESIS OBJECTIVE

The objective of this thesis is to design a suitable unit-cell pattern to be used on a structure to create an attenuation or induce absorption for a specific radar frequency. The application for this MTM will be to reduce the radar signature of ships and aircraft. The layers must be as thin and lightweight as possible. Unlike many other MTM applications, loss is desired for this RAM. The X-band (8–12 GHz) has been selected as the frequency band of interest for this study. Microwave Studio (MWS) software by CST was used to model different types of MTMs over the frequency band of interest.

D. THESIS OUTLINE

A brief introduction to military radar, the background of MTMs and a literature review were given in Chapter I. The unique properties of MTMs that emerge when they interact with EM waves are explained in Chapter II. Included in Chapter II is a brief history of a common type of MTM based on the split-ring resonator. Modeling and simulation of the various designs of MTM unit cell is done in Microwave Studio, as shown in Chapter III. The various results achieved are discussed and compared in Chapter IV. The conclusions of the research, recommendations on applications and suggestions for future studies are presented in Chapter V.

THIS PAGE INTENTIONALLY LEFT BLANK

II. METAMATERIALS

A. INTRODUCTION

In this chapter, the basic concepts of MTM are discussed. The first is what material and configurations are classified as MTM. The second is how MTM interacts with EM waves. For example, Snell's law of refraction, which refers to refraction encountered when EM waves or light passes from one medium to another must be amended. Third, there is the possibility of negative real parts of the permittivity and permeability, the two electrical parameters that define a medium.

B. DOUBLE-NEGATIVE MATERIAL

It should be pointed out that MTMs include a wide variety of synthetic materials with inclusions or structures. Often MTMs are referred to as double-negative material, although some can be single-negative (SNG). DNG refers to material with simultaneous negative real parts of the permittivity ε_r' and permeability μ_r'. The negative values found in MTMs give them the unique property of negative refraction (elaborated upon in the next section). The ε and μ of a material are usually expressed as their complex relative terms, as defined in Equations (1.1) and (1.2).

The imaginary parts of ε_r'' and μ_r'' are responsible for losses in the MTM due to electric and magnetic damping and finite conductivity [14]. MTMs fall into a variety of classifications, such as chiral, homogeneous, inhomogeneous, isotropic, anisotropic, and bianisotropic. In most materials, permittivity and permeability are described by scalar values. For anisotropic material, they can only be described by a matrix or dyadic. In matrix notation,

$$\varepsilon_r = \begin{pmatrix} \varepsilon_{xx} & \varepsilon_{xy} & \varepsilon_{xz} \\ \varepsilon_{yx} & \varepsilon_{yy} & \varepsilon_{yz} \\ \varepsilon_{zx} & \varepsilon_{zy} & \varepsilon_{zz} \end{pmatrix} \tag{2.1}$$

and

$$\mu_r = \begin{pmatrix} \mu_{xx} & \mu_{xy} & \mu_{xz} \\ \mu_{yx} & \mu_{yy} & \mu_{yz} \\ \mu_{zx} & \mu_{zy} & \mu_{zz} \end{pmatrix} \tag{2.2}$$

where the elements in the matrix are the complex relative values that fully describe the permittivity and permeability [15]. The vast majority of MTMs have only diagonal elements in Equations (2.1) and (2.2):

$$\varepsilon = \begin{pmatrix} \varepsilon_x & 0 & 0 \\ 0 & \varepsilon_y & 0 \\ 0 & 0 & \varepsilon_z \end{pmatrix}; \tag{2.3}$$

$$\mu = \begin{pmatrix} \mu_x & 0 & 0 \\ 0 & \mu_y & 0 \\ 0 & 0 & \mu_z \end{pmatrix}. \tag{2.4}$$

The permittivity and permeability for a lossless DNG material can also be written as [16]

$$\sqrt{\varepsilon_r} = \sqrt{-\left|\varepsilon_r'\right|} = j\sqrt{\left|\varepsilon_r'\right|} \tag{2.5}$$

and

$$\sqrt{\mu_r} = \sqrt{-\left|\mu_r'\right|} = j\sqrt{\left|\mu_r'\right|}. \tag{2.6}$$

Therefore, the wavenumber is [17]

$$k = \omega\sqrt{\varepsilon_o\varepsilon_r'}\sqrt{\mu_o\mu_r'} = -\omega\sqrt{\left|\varepsilon_o\varepsilon_r'\right|}\sqrt{\left|\mu_o\mu_r'\right|} = -\omega k_0\sqrt{\left|\varepsilon_r'\right|\left|\mu_r'\right|} \tag{2.7}$$

where $k_0 = \omega\sqrt{\mu_0\varepsilon_0} = \omega/c$ and $c = 2.998 \times 10^8$ m/s. The intrinsic impedance of the medium is

$$\eta = \eta_o\frac{\sqrt{\mu_r'}}{\sqrt{\varepsilon_r'}} = \eta_o\frac{\sqrt{\left|\mu_r'\right|}}{\sqrt{\left|\varepsilon_r'\right|}} \tag{2.8}$$

where $\eta_0 = \sqrt{\mu_0/\varepsilon_0}$.

C. RETRIEVAL OF ε AND μ FROM S_{11} AND S_{21}

To retrieve ε and μ, refer to the paper by Xudong Chen et al. [18], where the S-parameters are expressed in terms of the reflection and transmission coefficients as

$$S_{11} = R \tag{2.9}$$

and

$$S_{21} = Te^{jk_0 d} \tag{2.10}$$

where d is the thickness of the material under test. The wave impedance Z and the refractive index n are related to S_{11} and S_{21} by

$$Z = \pm\sqrt{\frac{(1+S_{11})^2 - S_{21}^{\,2}}{(1-S_{11})^2 - S_{21}^{\,2}}} \tag{2.11}$$

and

$$n = \frac{1}{k_0 d}\left\{\left[\mathrm{Im}\left[ln\left(e^{jnk_0 d}\right)\right] + 2m\pi\right] - j\left[\mathrm{Re}\left[ln\left(e^{jnk_0 d}\right)\right]\right]\right\} \tag{2.12}$$

where m is an integer related to the branch index of the real part of n. The value of $e^{jnk_0 d}$ is derived from

$$e^{jnk_0 d} = \frac{S_{21}}{1 - S_{11}\dfrac{Z-1}{Z+1}}. \tag{2.13}$$

In reference [18], it is also mentioned that the correct sign of Z can be determined by the relationship of Z and n. Two cases to correctly find the sign of Z are identified. The first case is for $\left|\mathrm{Re}(Z)\right| \geq \delta$, where δ is positive and for which $\mathrm{Re}(Z) \geq 0$. The second case is to choose the sign of Z so that the corresponding $\mathrm{Im}(n) \geq 0$, or $\left|e^{jnk_0 d}\right| \leq 1$. The method to accurately determine the branch of $\mathrm{Re}(n)$ is described in [18]. With Z and n determined, ε can be found from the relation

$$\varepsilon = \frac{n}{Z} \tag{2.14}$$

and μ found from

$$\mu = nZ\,. \tag{2.15}$$

D. NEGATIVE REFRACTION AND LEFTHANDEDNESS

The phenomenon of negative refraction is usually illustrated with an obliquely incident wave from a double-positive (DPS) material into a double-negative material and exiting to a double-positive material, as illustrated in Figure 4. Snell's law for a lossless DPS-DNG boundary can be written as

$$\frac{\sin\theta_i}{\sin\theta_r} = \frac{n_1}{-n_2}. \tag{2.16}$$

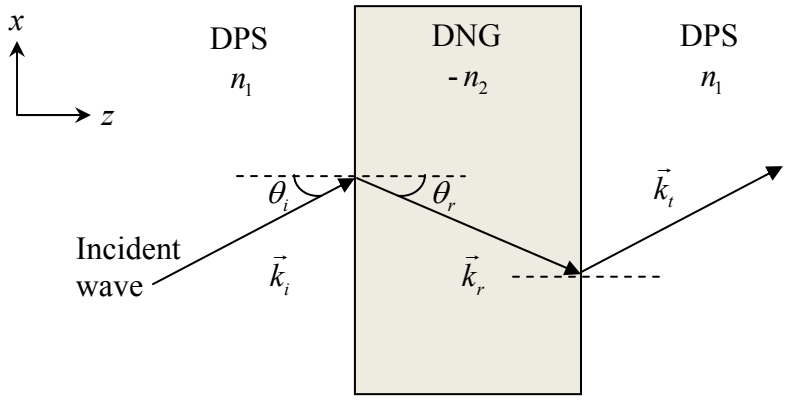

Figure 4. Obliquely incident wave propagation from DPS-DNG-DPS. Notice that the wave bends to the same side as the incident wave (After [19]).

The wave vectors (ray directions) for the incident, reflected, and transmitted fields are [19]

$$\begin{aligned} \vec{k}_i &= k_1\left(\cos\theta_i\hat{z} + \sin\theta_i\hat{x}\right) \\ \vec{k}_r &= k_1\left(-\cos\theta_i\hat{z} + \sin\theta_i\hat{x}\right) \\ \vec{k}_t &= k_2\left(\cos\theta_t\hat{z} + \sin\theta_t\hat{x}\right) \end{aligned} \tag{2.17}$$

where $k_1 = \omega\sqrt{\mu_1\varepsilon_1}$ and $k_2 = \omega\sqrt{\mu_2\varepsilon_2}$.

The Poynting vectors are

$$\vec{S}_i = \frac{1}{2}\frac{|E_o|^2}{\eta_1}\left(\cos\theta_i\hat{z} + \sin\theta_i\hat{x}\right)$$

$$\vec{S}_r = \frac{1}{2}\frac{|RE_o|^2}{\eta_1}\left(-\cos\theta_i\hat{z} + \sin\theta_i\hat{x}\right) \tag{2.18}$$

$$\vec{S}_t = \frac{1}{2}\frac{|TE_o|^2}{\eta_2}\left(\cos\theta_t\hat{z} + \sin\theta_t\hat{x}\right)$$

where *R* and *T* are the reflection and transmission coefficients, respectively, and E_o is the amplitude of the incident wave. The impedances are defined in accordance with Equation (2.8).

When waves propagate in DPS materials, the Poynting vector and wavefront velocity vector are in the same direction. If a wave propagates in a DNG material with a negative index, the Poynting and wave vectors are

$$\vec{k}_t = -|n_2|\frac{\omega}{c}\left(\cos|\theta_t|\,\hat{z} - \sin|\theta_t|\,\hat{x}\right) \tag{2.19}$$

and

$$\vec{S}_t = \frac{1}{2}\frac{|TE_o|^2}{n_2}\left(\cos|\theta_t|\,\hat{z} - \sin|\theta_t|\,\hat{x}\right). \tag{2.20}$$

These equations show that the wave vector points in the opposite direction of the power flow, the Poynting vector being directed in a causal direction away from the interface. This property is referred to as lefthandedness.

E. SPLIT-RING RESONATOR

Much current research and experimentation is based on the SRR. It is a good structure to illustrate how the magnetic properties of a MTM are achieved. The SRR design was derived from square arrays of concentric cylinders, as proposed by Pendry et al. in 1999 [20]. The structure is made of metallic films wound on a cylinder, but with a discontinuity (an axial slit) to prevent current from flowing azimuthally around the

cylinder, as seen in Figure 5. The metallic films are separated by a small distance to create capacitance that allows current to flow, as depicted in Figure 6.

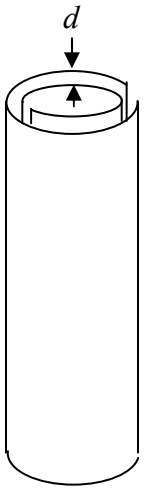

Figure 5. Cylinders with internal structures. Metallic films separated by distance *d*. There is a small gap at every film that prevents current from flowing around the "ring" (From [20]).

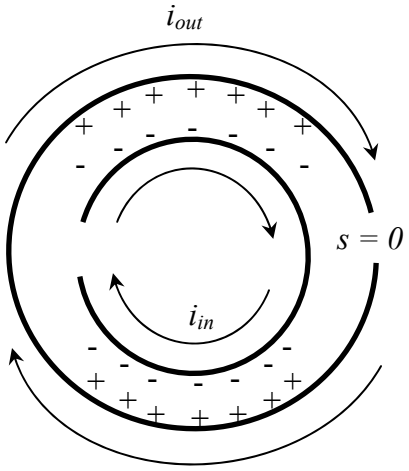

Figure 6. Plan view of the cylinder. When the cylinder encounters a magnetic field parallel to it, current is induced. Current is proportional to the capacitance of the structure (After [20]).

The capacitance in the structure balances out the inductance present when the cylinder is placed in a square array. The metallic cylinders in the square array induce

current along the length of the cylinder if an electric field is not parallel to it. This creates undesirable anisotropic behavior. To obtain isotropic behavior, the structure is modified to have a series of flat disks that retain the split-ring configuration. They can be observed as the concentric square structure in Figure 2. They are also referred to as coplanar rings (CPRs).

The structure of the SRR exhibits negative permeability, while an array of wires exhibits negative permittivity. To create a structure with both negative permittivity and permeability, a wire is inserted behind the SRR [11], as shown in Figure 2. This represents an example of V. G. Veselago's left-hand material, as demonstrated by Smith et al. in 2001 [10].

F. SUMMARY

The theory and formulation of double-negative materials and the propagation of EM waves in a material with negative refractive index were presented in this chapter. The working principle of a common design of MTM, the SRR, was reviewed. In the next chapter, the modeling of the MTM design in MWS and the simulation setup parameters are explained.

THIS PAGE INTENTIONALLY LEFT BLANK

III. MODELING AND SIMULATION SETUP

A. INTRODUCTION

Using a computer simulation for product design greatly enhances productivity and reduces the time and cost of research. The computer simulation program of choice was MWS by CST. In this research, different MTM designs are simulated, and the original design from [22] is modified to improve performance. The modeling of MTM designs and the setup of the parameters used in simulations are described in detail in this chapter.

B. CST MICROWAVE STUDIO (MWS)

MWS was chosen because it provides fast, efficient analysis and design of EM components, including printed circuit boards (PCBs). This software is based on the finite integration technique (FIT) that requires the discretization of the entire calculation volume. The calculation volume includes the MTM structure plus some additional surrounding free space.

The software is capable of importing designs and diagrams drawn in other software formats. MWS parameterizes imported CAD files. It uses an advanced ACIS-based parametric modeling front end with structure visualization, and the software also has a materials database.

MWS has multiple solvers: transient (time domain), frequency domain, eigenmode, integral equation, multilayer, and hybrid (ray tracing). The transient solver in MWS is the main simulation mode used for this research. This solver is suitable for most high frequency applications and can obtain the entire broadband frequency behavior of the simulated device in just one calculation run. An excellent feature in the transient solver is the linear scaling of computational resources with structure size. This feature allows the calculation of large arrays of elements based on a unit-cell design where periodicity of the structure is taken into account [21].

C. BASELINE DESIGN

The model for this research was based on a design described in [22], shown in Figure 7. This particular design is appealing because of its simultaneous absorption and low reflection. It is a window structure designed to operate with free-space on both sides. Part of the design modification is to make this structure operate as a coating over a platform surface. The selected frequency is 11.5 GHz.

The design is derived from conventional coplanar rings and wires. Electric coupling was supplied from the electric-ring resonator (ERR) [23]. The structure in Figure 7(a) can be considered two coplanar split rings connected by the inductive ring parallel to the split wire. This design was used instead of a conventional split-wire design because a split-wire design is limited, other than the addition of more wires per unit cell, for increasing its inductance [24]. Magnetic coupling was created with flux from the circulating charges perpendicular to the propagation vector. This response was created by combining the center wire of the ERR with a cut wire separated by the substrate, as shown in Figures 7(b) and 7(c). The magnetic response can be tuned by changing the geometry of the cut wire and substrate thickness. By manipulating the magnetic coupling without changing the ERR, permittivity and permeability can be decoupled, and each resonance can be individually tuned [22]. The dimensions (in millimeters) as given in the paper are listed in Table 2.

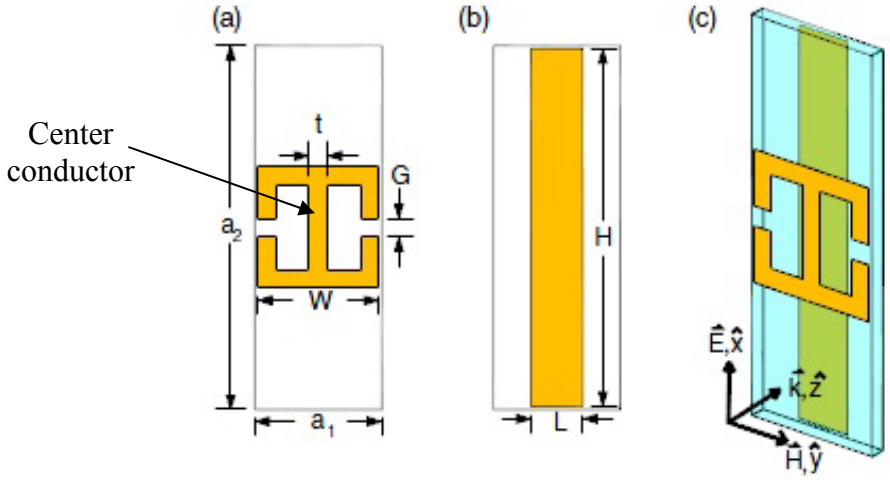

Figure 7. (a) A front view of the resonator, (b) back view of the wire and (c) oblique view of the unit cell with direction of propagation in *z* (From [22]).

Table 2. Value of parameters used in the design from [22].

Parameter	Dimension (mm)
a_1	4.2
a_2	12.0
W	3.9
G	0.606
t	0.6
L	1.7
H	11.8
Conductor thickness	0.017
Substrate thickness	0.2
Wire thickness	0.017
Separation distance between layers	0.65
Number of unit cell layers	2 pieces

The authors state that FR-4 is used as the substrate, but they did not specify the permittivity and loss tangent. Typical values for the permittivity of FR-4 range from 3.65 to 5.20. The loss tangent ranges from 0.013 to 0.025. In the simulations, a permittivity of 4.4 and loss tangent of 0.021 were used. In the many simulations that follow, it was noticed that the loss tangent did not have much of an effect on the results. The permittivity of the substrate has a noticeable effect on the results. Generally, when the permittivity of the substrate was increased in simulations, the reflection coefficient scattering parameter S_{11} increased while the transmission coefficient scattering parameter S_{21} decreased. The opposite happened when permittivity was decreased. The specific values are not critical, as it is possible to redesign the MTMs to give low S_{11} and low S_{21}. Therefore, a medium value of 4.4 was chosen for permittivity.

The frequency for the transient solver spans 0 to 25 GHz. The settings in MWS for the boundary conditions and background properties used in simulations are as per Figure 8 (a) and (b), respectively. A simulation was run in MWS, which gave good agreement with the published results.

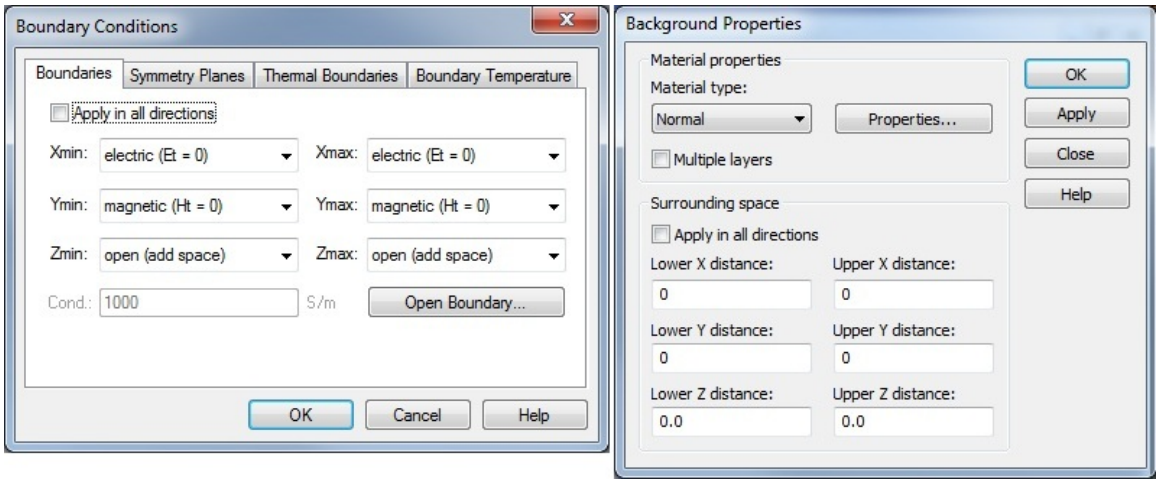

(a) (b)

Figure 8. (a) Setup of the boundary conditions and (b) background properties used in MWS simulations (From [21]).

Different values and combinations of the parameters *L, H, t* (in Figure 7) and the separation of the substrate were tested to observe the results. Generally, the achieved results are near the frequency for absorption or absorption level of the results reported in [22].

A variety of modifications to the design in [22] were done, and some are shown in Figure 9. In all, the different values of the thickness, width of conductor, and separation of substrate in the new designs were tested. The most promising results are seen in Figure 9 (c) and (e), so more testing was done on these two designs. Other boundary conditions for the simulation, as described in detail in the next section, were also applied to make sure that the results converged and are consistent.

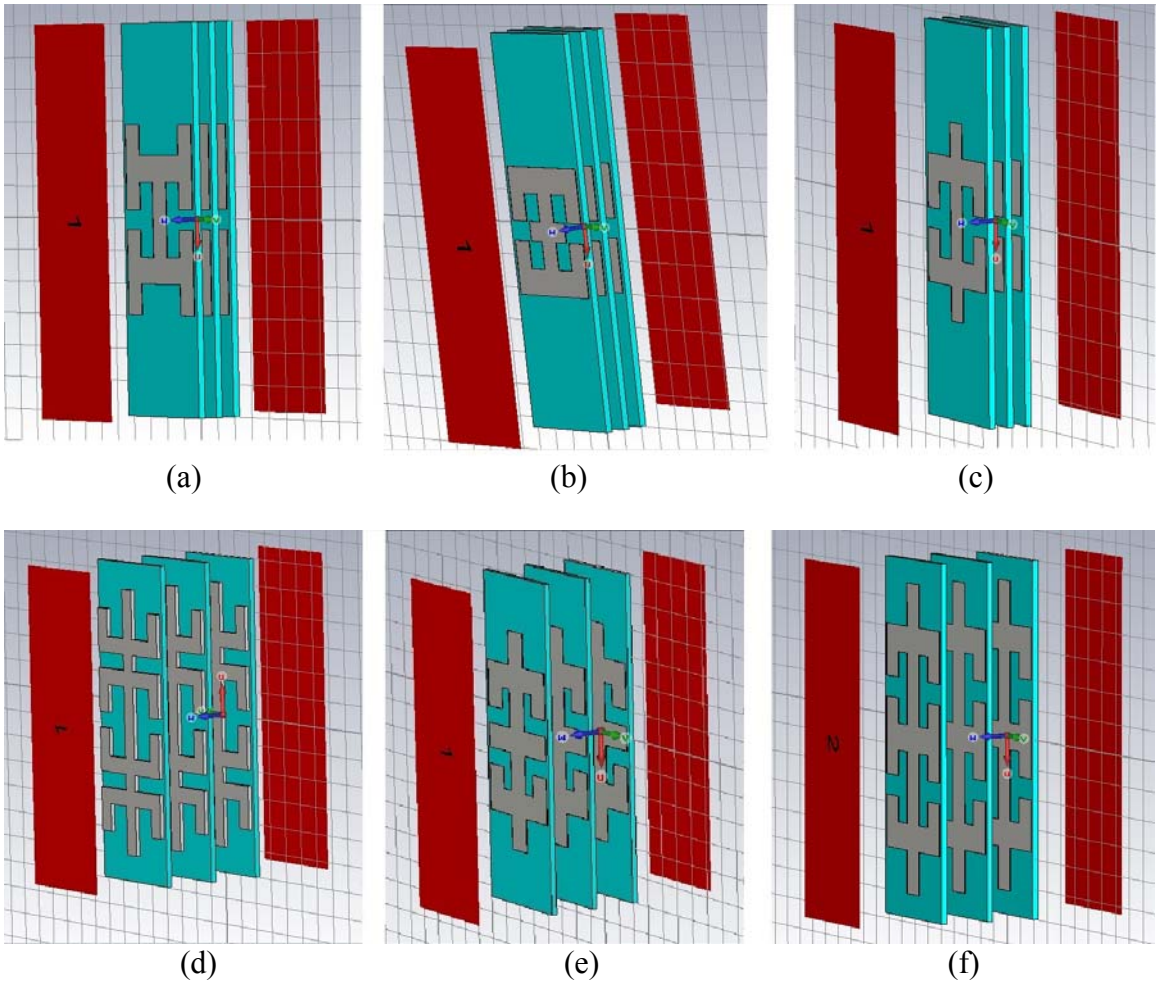

Figure 9. Several variations of the baseline design (a)–(f) that were tested. As shown here, three pieces of each design were simulated with waveguide ports.

D. OTHER BOUNDARY CONDITIONS

The initial testing for all the designs was done with the boundary conditions as in Figure 8 (a) and simulated using the transient solver. The boundary conditions have $E_{tan} = 0$ on the X_{max} and X_{min} sides and $H_{tan} = 0$ on the Y_{max} and Y_{min} sides. This simulates a plane wave with E_x and H_y. This configuration can only simulate normal incident angles but can do a broadband calculation of S-parameters from one single calculation run by applying discrete Fourier transforms to the time signals [21]. This configuration was also

used with the frequency domain solver to verify convergence and accuracy. The frequency domain solver has options for periodic boundary conditions and the use of Floquet modes for non-normal incidence angles.

1. Periodic Boundary Condition

Periodic boundary conditions are used to simulate an infinite structure of the unit-cell design. This is done in the frequency-domain solver. For this mode of simulation, in the "Boundary Conditions" setting box, the X_{min}, X_{max}, Y_{min} and Y_{max} are set to "Periodic." Z_{min} and Z_{max} are set to "Open (add space)."

2. Unit-cell Boundary Condition

Floquet modes are used to simulate oblique angles of incidence on the infinite structure of the design. This is done in the frequency-domain solver. This approach can obtain accurate results at very oblique angles of incidence (close to grazing) [25]. For this mode of simulation, in the "Boundary Conditions" setting box, the X_{min}, X_{max}, Y_{min} and Y_{max} are set to "Unit Cell." Z_{min} and Z_{max} are set to "Open (add space)." Different "Theta" and "Phi" angles for simulation can also be specified in "Phase Shift/Scan Angles."

E. PORTS

Optimization of the parameters of the design is done with two ports, one in front, facing the three-layered unit cell, and one behind, facing the back of the three-layered unit cell. The ports are where the model is excited (stimulated) and the response (output) fields monitored. This configuration, depicted in Figure 10, is to compute the reflection coefficient S_{11} and transmission coefficient S_{21} parameters. S_{11} and S_{22} are the reflection coefficients of the material under test (e.g. S_{11} means transmitting from port 1 and receiving at port 1). S_{12} and S_{21} refer to the transmission coefficients of the material under test. (e.g. S_{12} means transmitting from port 2 and receiving at port 1).

The layer or coating configuration, shown in Figure 11, uses only one port, the one that faces the unit cell from the front. The back of the three-layered unit cell has a

metallic plate 0.85 mm away. This is used to simulate the actual application where the MTM structure is applied onto the platform as a coating. The skin of the platform is the metallic plate.

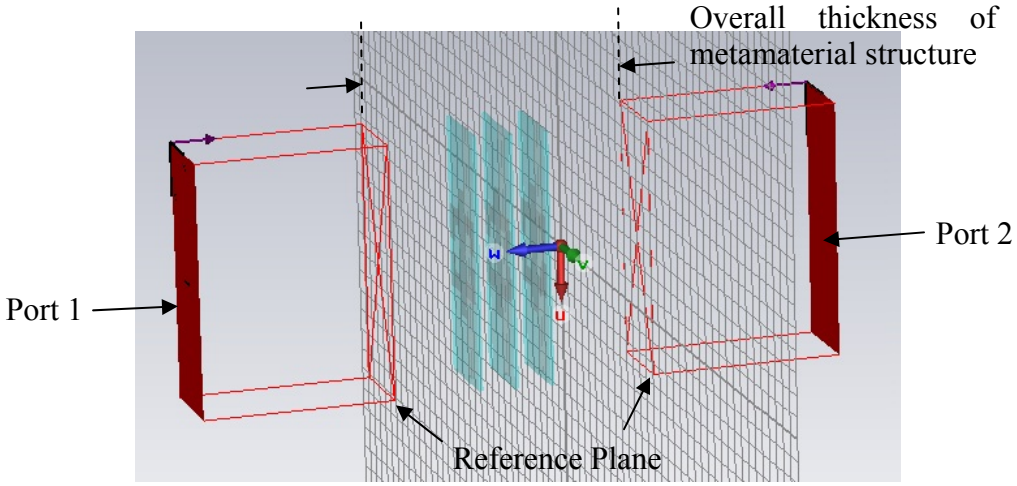

Figure 10. Two-port configuration used to compute the S_{11} and S_{12} parameters.

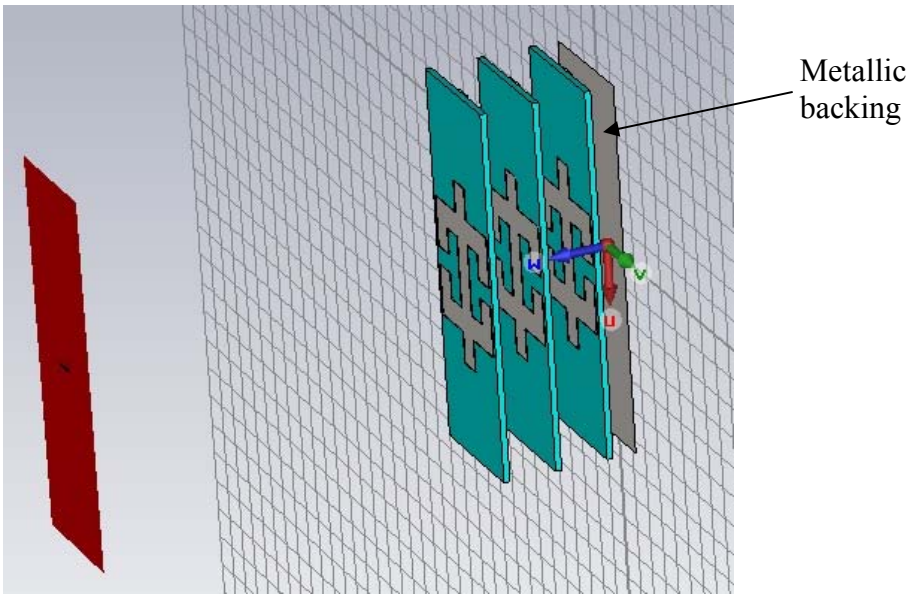

Figure 11. Single port configuration used to compute S_{11} for a coating application.

F. THE REFERENCE PLANE

The distance between the reference planes of the two ports defines the electrical thickness of the whole MTM structure. The reference plane can be specified when defining the ports. The phase and amplitude references for S_{11} and S_{12} are taken at the point where the reference plane is defined, which is not necessarily at the port. If no reference planes are defined, the references are taken at ports 1 and 2. The results for the simulations in the next chapter are taken with the reference planes defined at 4 mm away from the unit cell, as shown in Figure 12.

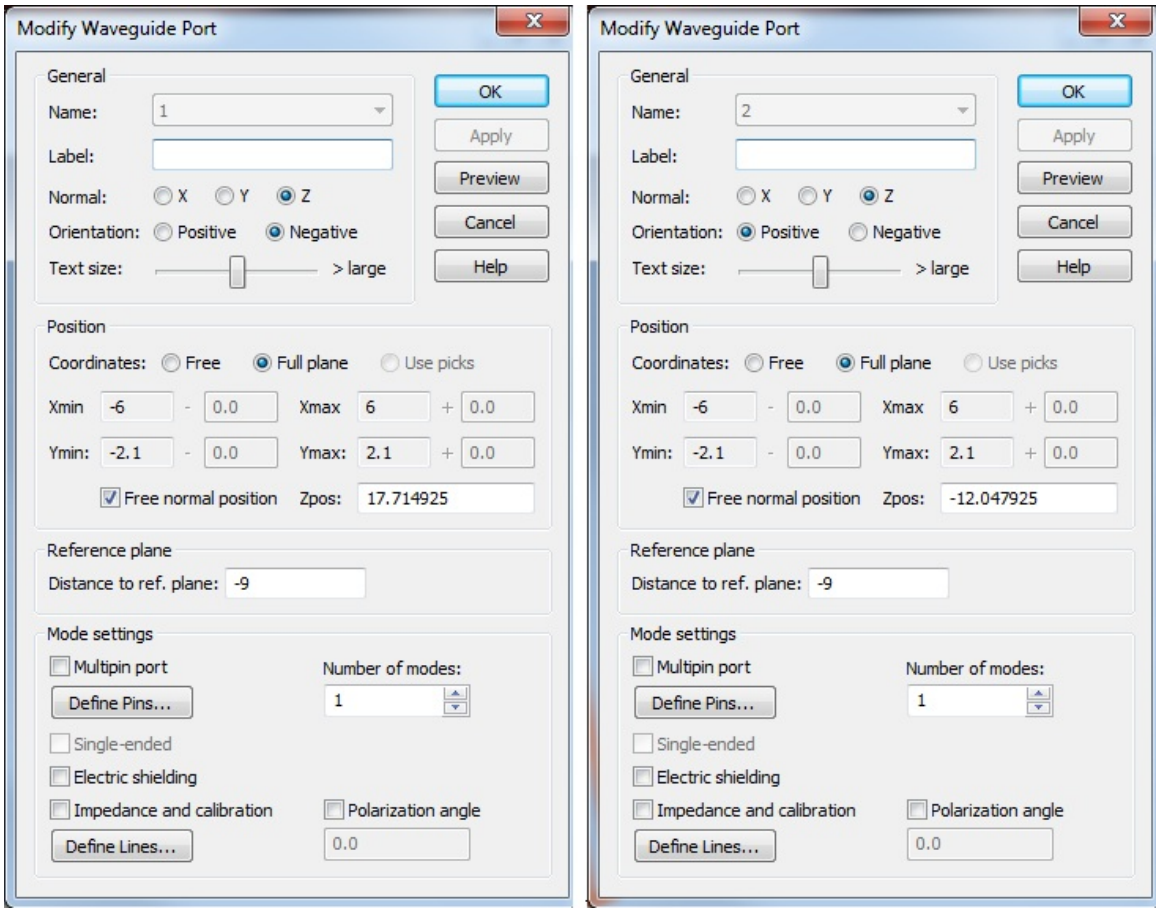

(a) (b)

Figure 12. (a) Definition of waveguide port 1. (b) Definition of waveguide port 2.

In this chapter, the modeling details of the MTM and the setup configurations for simulations in MWS using different boundary conditions were described. In the next chapter, the results obtained in the simulations are presented and analyzed.

THIS PAGE INTENTIONALLY LEFT BLANK

IV. SIMULATION RESULTS AND DATA ANALYSIS

The simulation results for two main MTM designs that came closest to the performance objectives are presented in this chapter. An explanation of the different parameters that are tuned to achieve the desired results is also included.

A. DESIGN (C)

As mentioned, the baseline design for this research is based on [22], shown in Figure 9 (c). Subsequently we refer this as Design (c). Modifications were made to several of the parameters. The final design has maximum absorption at 11.5 GHz, close to 11.65 GHz of [22]. The final dimensions of Design (c) are shown in Table 3. The CST model is shown in Figure 13. How the final design was derived are explained in the following sections.

Table 3. Final parameters used in simulation for the results of Design (c). Parameters are defined in Figure 7.

Parameter	Dimension (mm)
a_1	4.2
a_2	12.0
W	3.9
G	0.606
t	0.8
L	0.64
H	11.8
Conductor thickness	0.017
Center Conductor Length	6.0
Substrate thickness	0.2
Wire thickness	0.15
Separation distance between layers	1.7
Number of unit-cell layers	3 pieces

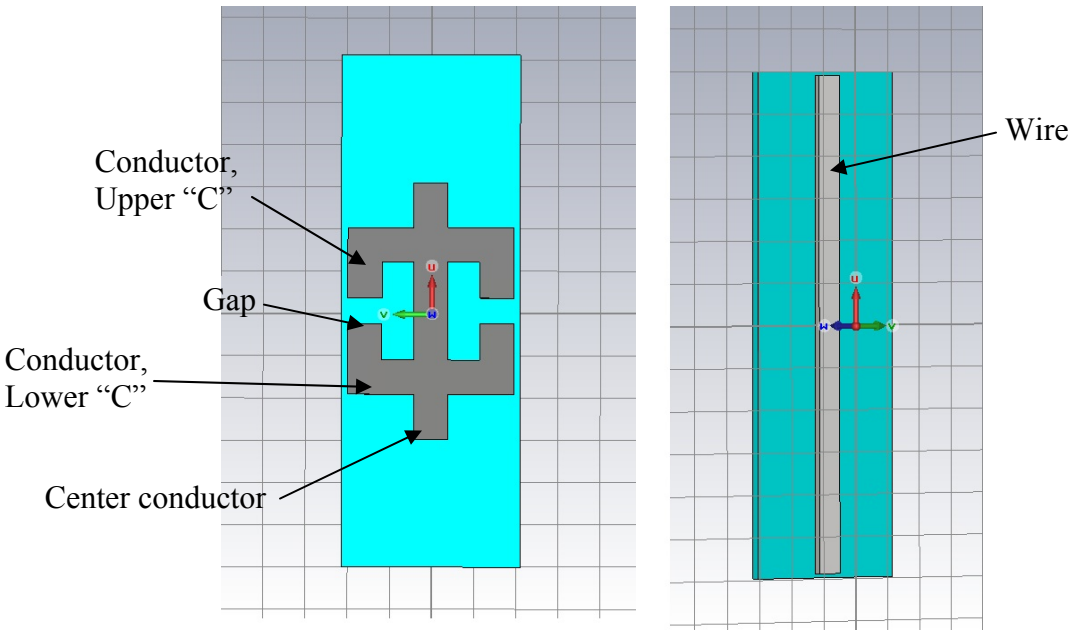

Figure 13. Design (c): the final design.

1. Length of Wire

Three simulations whose S_{22} and S_{12} results are depicted in Figures 14–16, are for substrates of lengths 8 mm, 12 mm, and 16 mm, respectively. The wire on the backside was 0.2 mm shorter than the substrate. The results in Figures 14–16 were simulated with the parameters in Table 3 (Figure 7), except *H*. As seen in Figure 14, when the wire is short, there is a peak of transmittivity (S_{12}) close to 11 GHz. As the length of the wire increases, this peak shifts to a lower frequency. The size of the unit cell was to be kept compact, so a long wire as in Figure 16 was not favorable. A long wire creates high reflectivity (S_{22}). The best result is seen in Figure 15, where there is low S_{12} at the frequency where S_{22} is the smallest of the three lengths. This means that the reduction in S_{22} is not due to the material being transparent to the EM wave, but rather to the material's more efficient absorption of EM waves at 11.5 GHz. Notice the peak absorption shifts to a higher frequency as the length of wire increases.

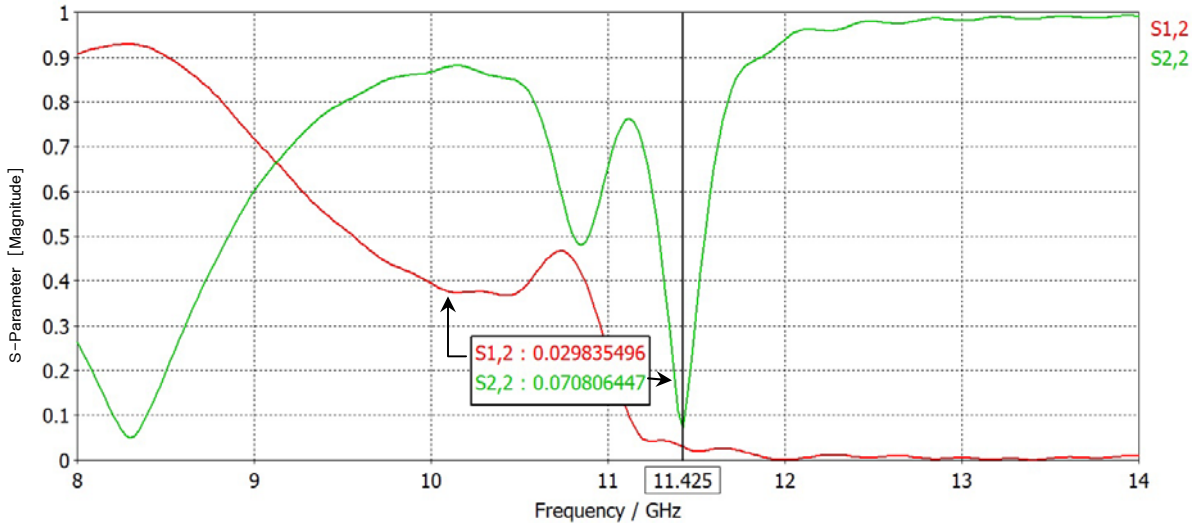

Figure 14. Simulated S-parameters for a wire of 7.8 mm in length.

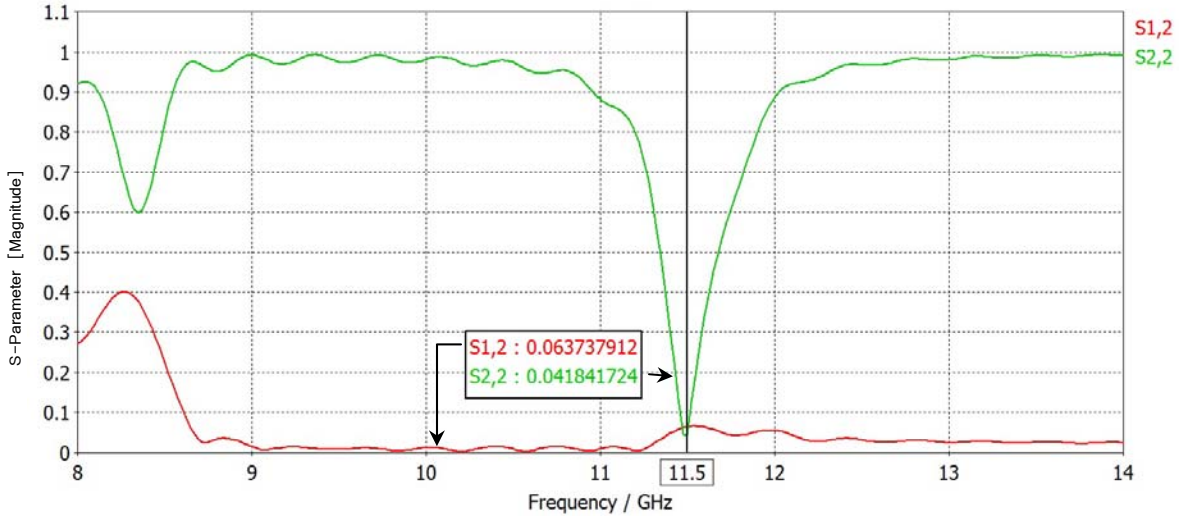

Figure 15. Simulated S-parameters for a wire of 11.8 mm in length (optimum).

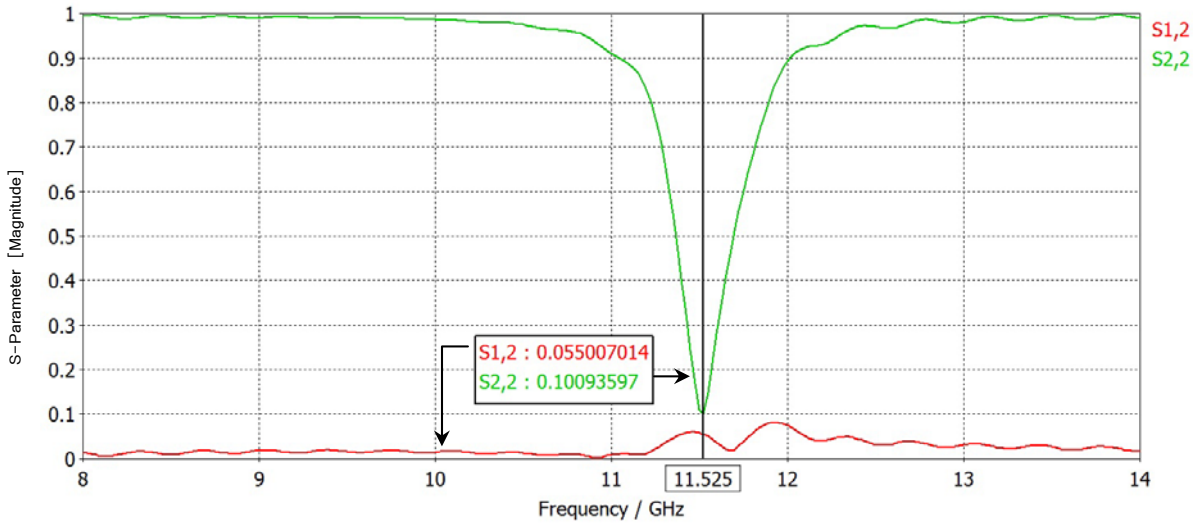

Figure 16. Simulated S-parameters for a wire of 15.8 mm in length.

2. Width of Wire

The results in Figures 17–20 were simulated with parameters as in Table 3, except wire width *L*. They show that the wire width also has an impact on the results. As the wire gets thinner, S_{22} decreases until the wire is 0.64 mm. When the width is less than 0.64 mm, S_{22} increases. The null also shifts to a higher frequency with reduced width. This is one of the parameters that can be used to tune the structure for the frequency of absorption.

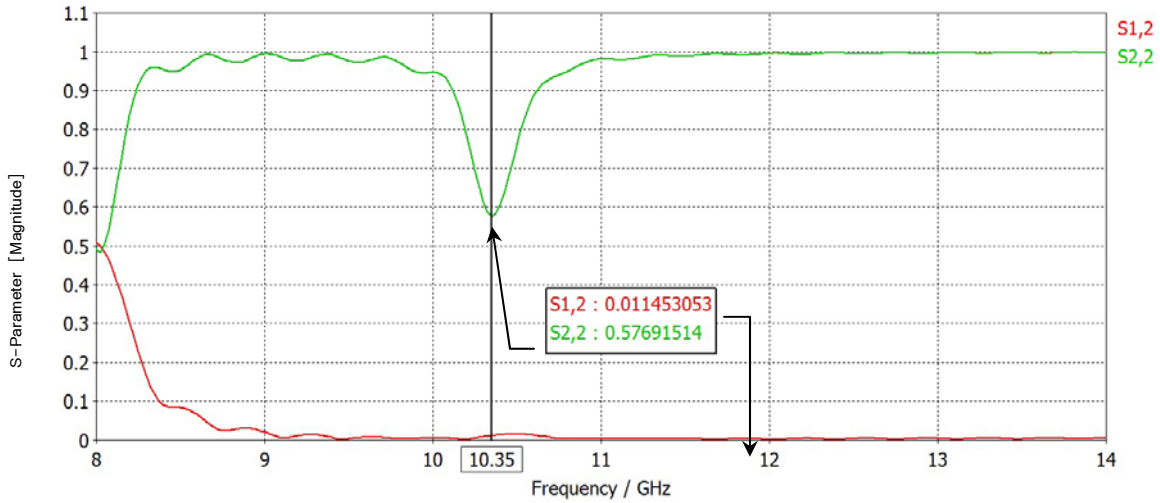

Figure 17. Simulated S-parameters for a wire width of 1.7 mm, as used in [22].

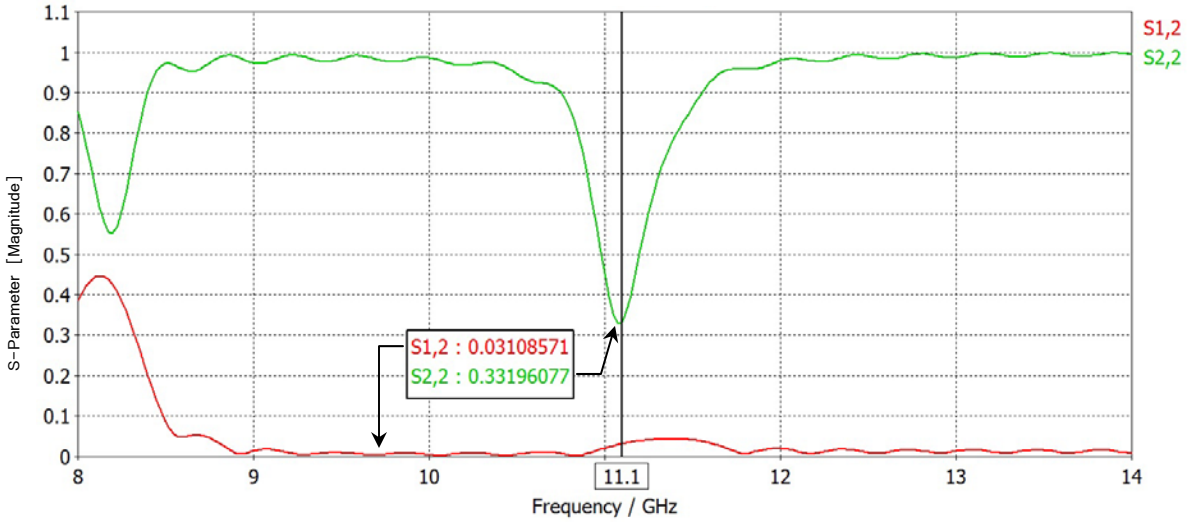

Figure 18. Simulated S-parameters for a wire width of 1.0 mm.

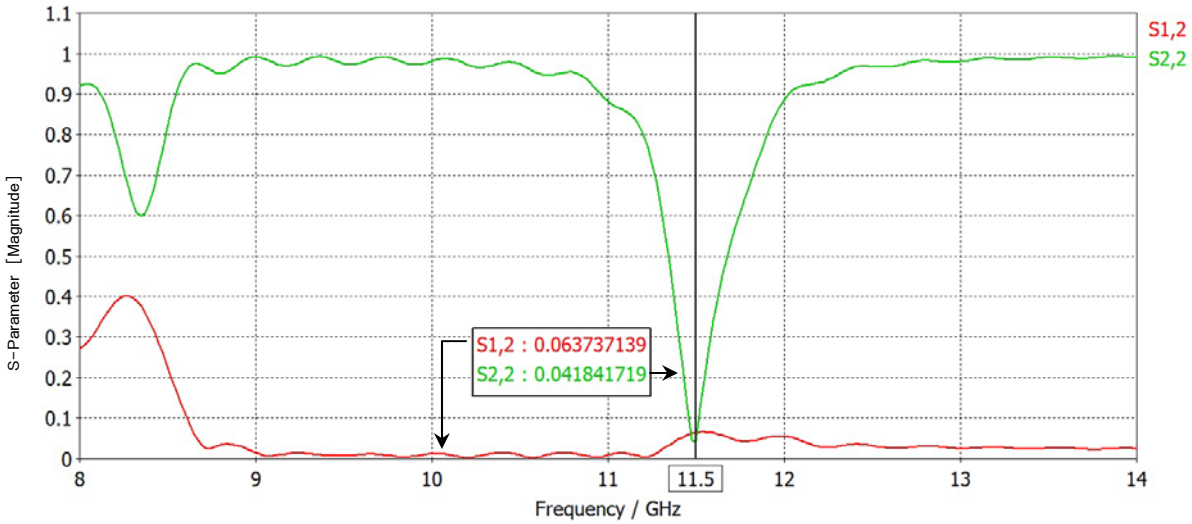

Figure 19. Simulated S-parameters for a wire width of 0.64 mm.

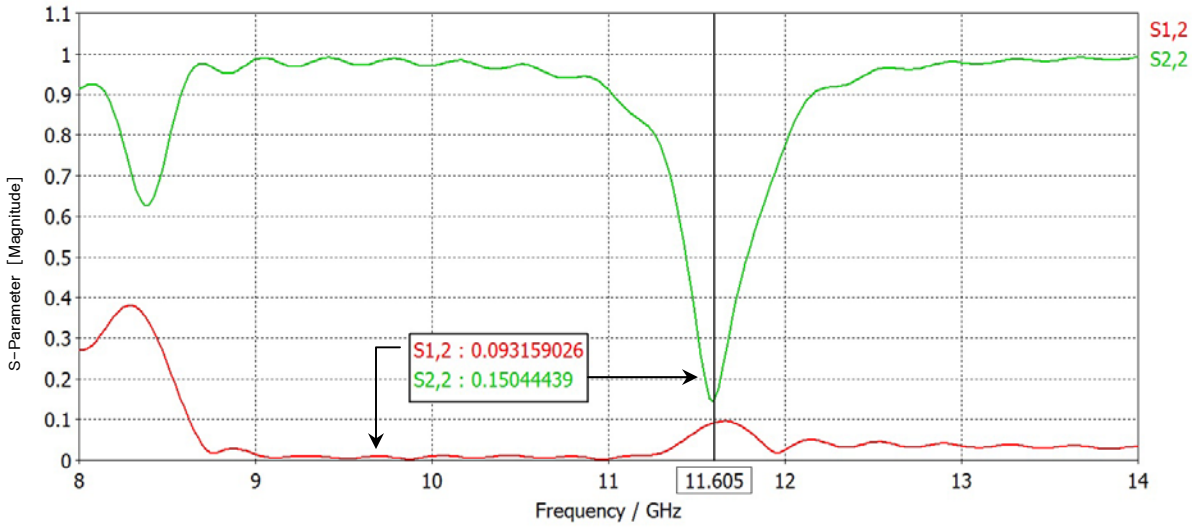

Figure 20. Simulated S-parameters for a wire width of 0.5 mm.

3. Thickness of Wire and Separation Distance Between Unit Cells

The effect of increasing the thickness of the wire and separation distance can be seen in Figures 21–23. Notice that the frequency location of the S_{22} null shifts higher as wire thickness and separation distance increased.

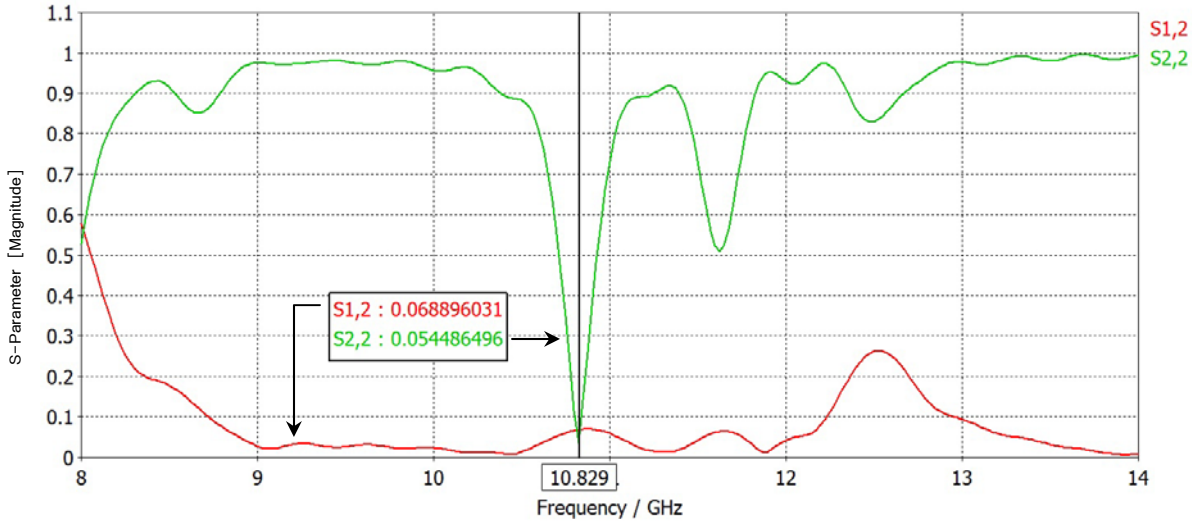

Figure 21. Simulated S-parameters for a wire thickness of 0.017 mm with unit-cell separation of 0.65 mm.

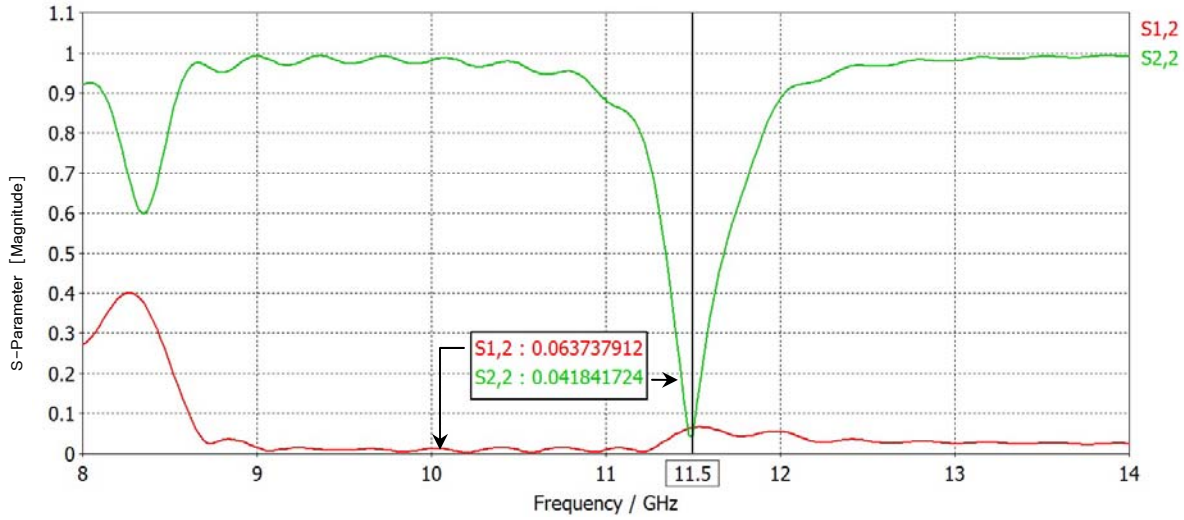

Figure 22. Simulated S-parameters for a wire thickness of 0.15 mm with unit-cell separation of 1.7 mm.

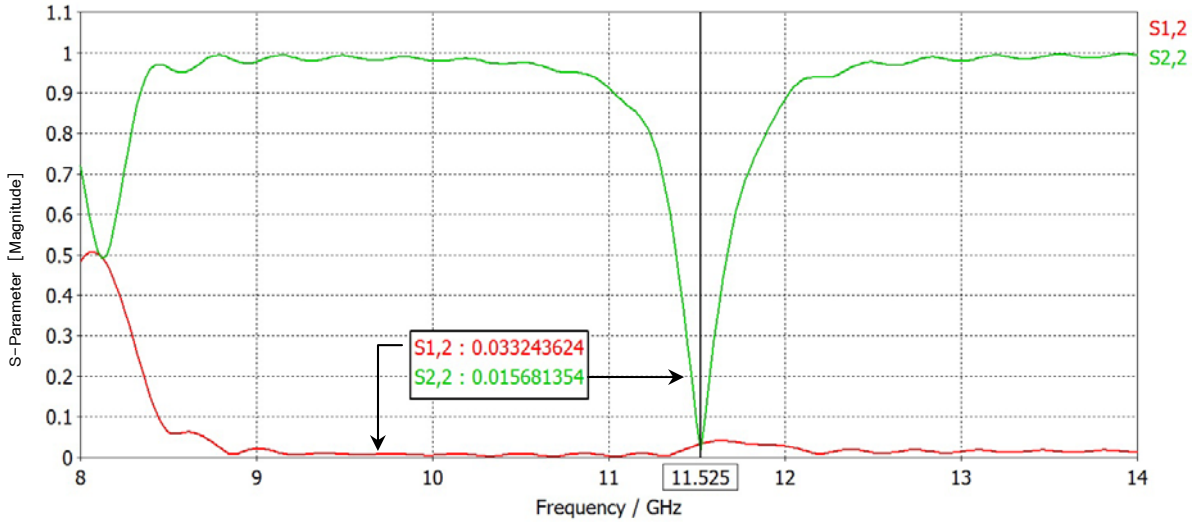

Figure 23. Simulated S-parameters for a wire thickness of 0.35 mm with unit-cell separation of 2.0 mm.

4. Number of Layers

The results for different numbers of unit-cell layers are shown in Figures 24–26. With two layers, the magnitude of the S_{22} is 0.062 as compared to a magnitudes of 0.042 and 0.035 for three and four layers, respectively. Three layers of unit cells were chosen as optimal because the difference in the result, compared with that of four layers, was very small, and the requirement is to keep the thickness as small as possible. The fewer layers there are, the less weight and thickness.

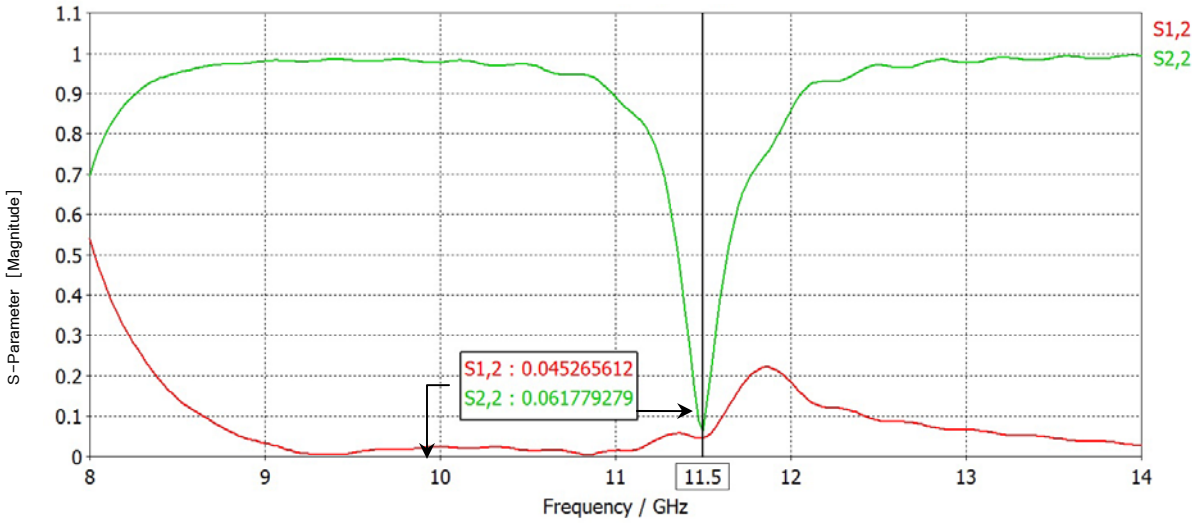

Figure 24. Simulated S-parameters for two layers.

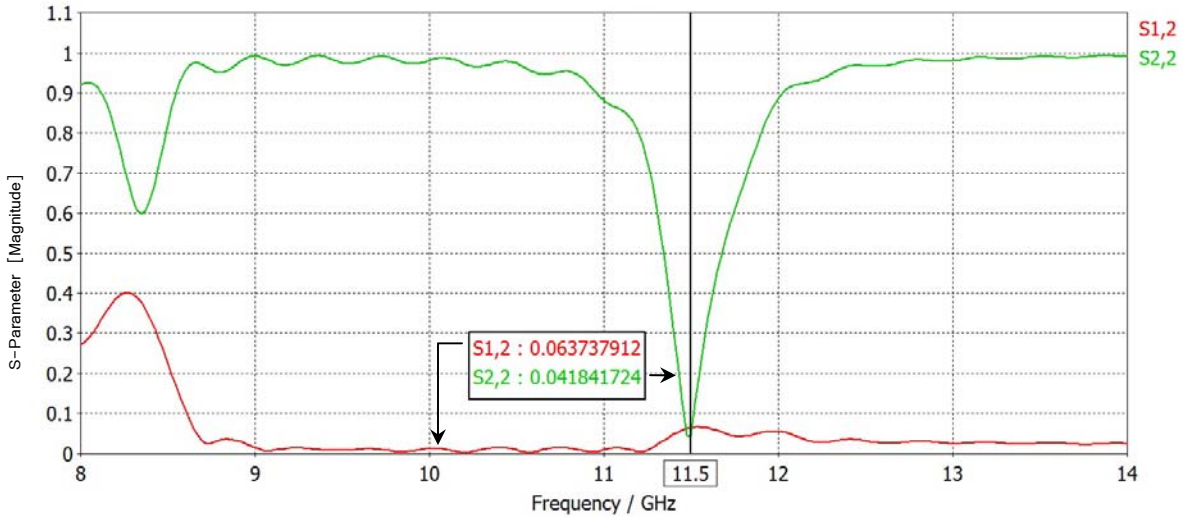

Figure 25. Simulated S-parameters for three layers.

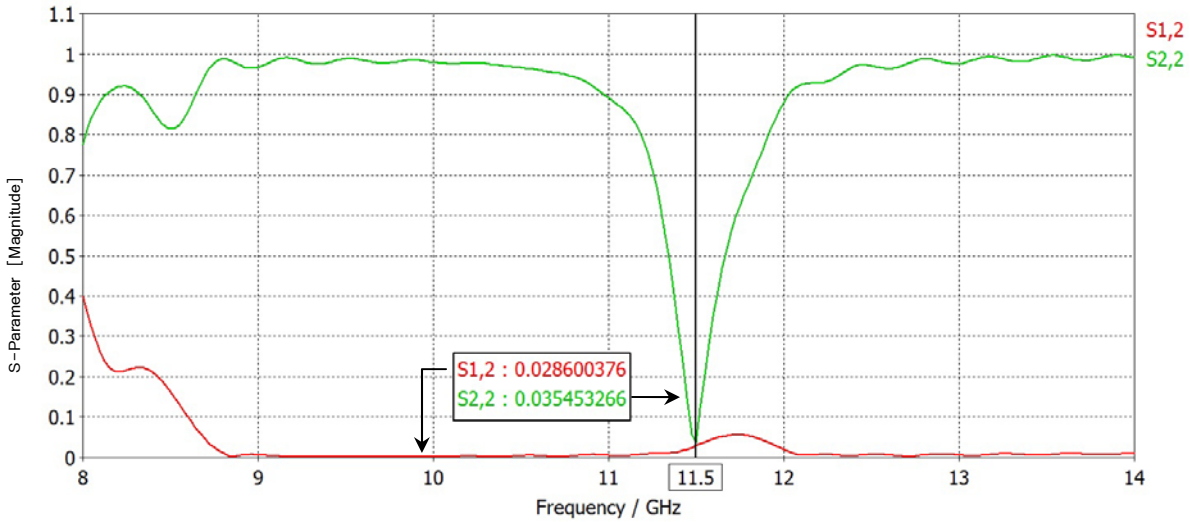

Figure 26. Simulated S-parameters for four layers.

5. Conductor Width

Next, the conductor width is varied keeping all other parameters constant. The effect of changing the width of conductor *t* is shown in Figures 27–29. It is seen that the optimal width lies at 0.8 mm.

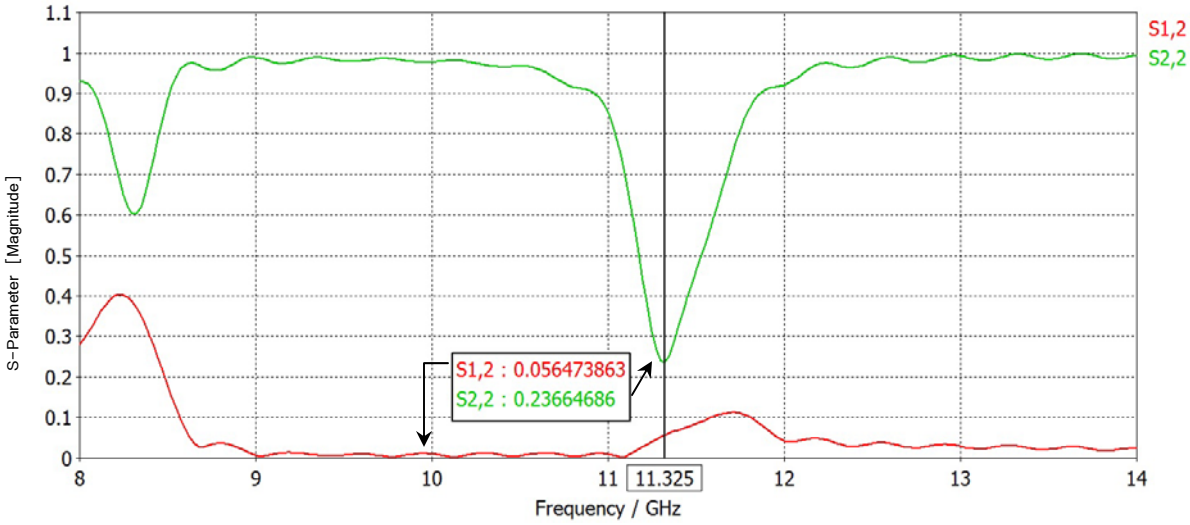

Figure 27. Simulated S-parameters for a conductor width of 0.6 mm.

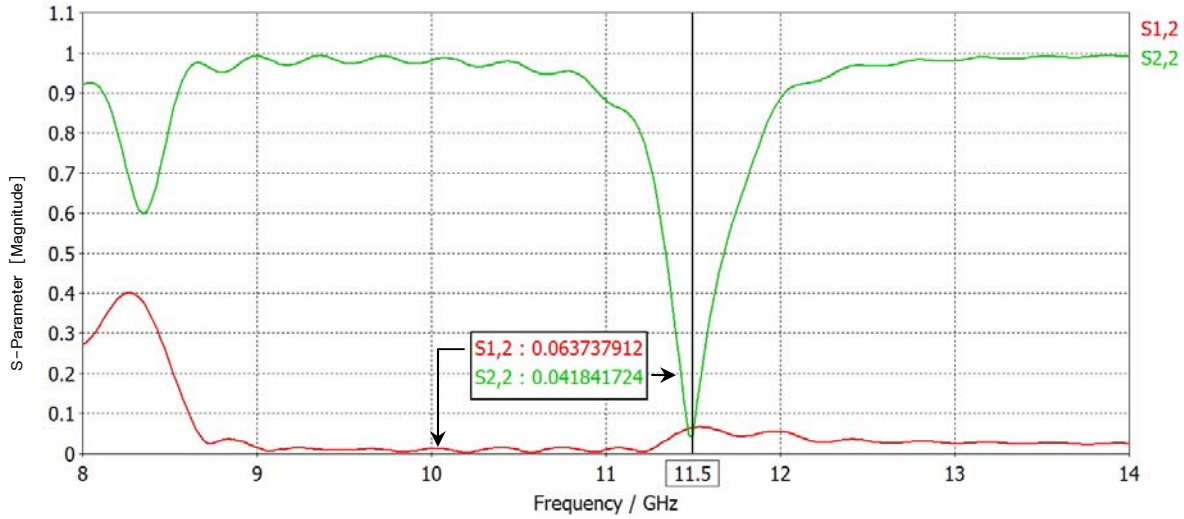

Figure 28. Simulated S-parameters for a conductor width of 0.8 mm.

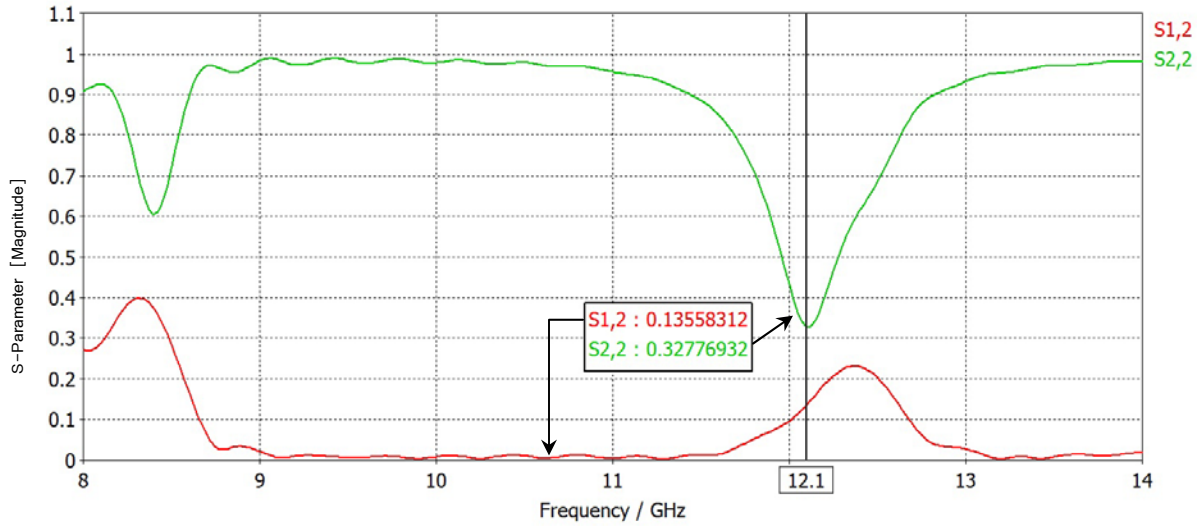

Figure 29. Simulated S-parameters for a conductor width of 1.0 mm.

6. Conductor Thickness

The effect of conductor thickness on the S-parameters is shown in Figures 30 and 31. Increasing the thickness of the conductor did not give a better result because of the increase in resistance. Therefore, the conductor thickness remains per the design in [22], $t = 0.017$ mm.

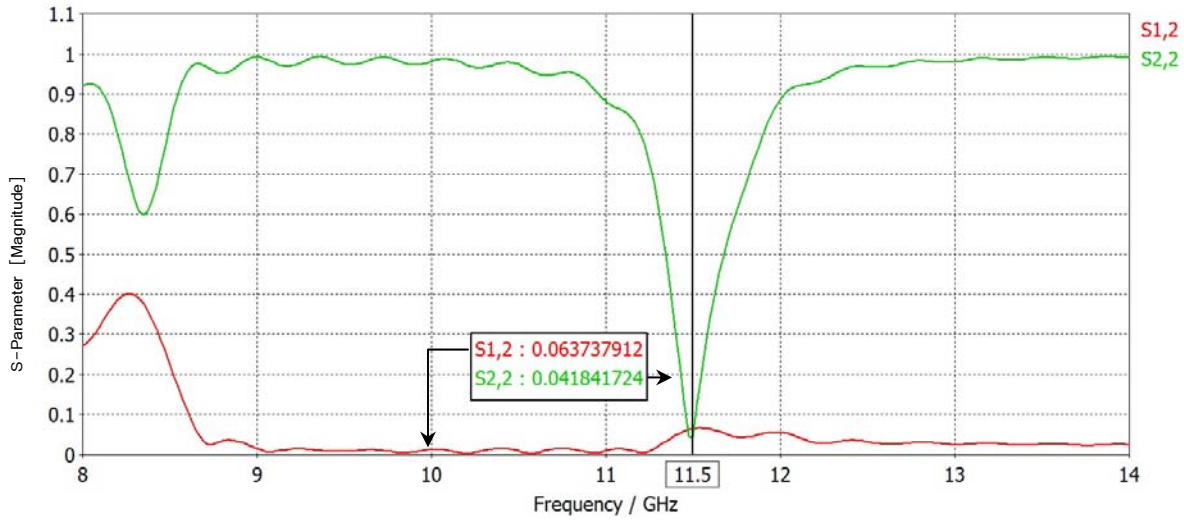

Figure 30. Simulated S-parameters for a conductor thickness per original design, 0.017 mm.

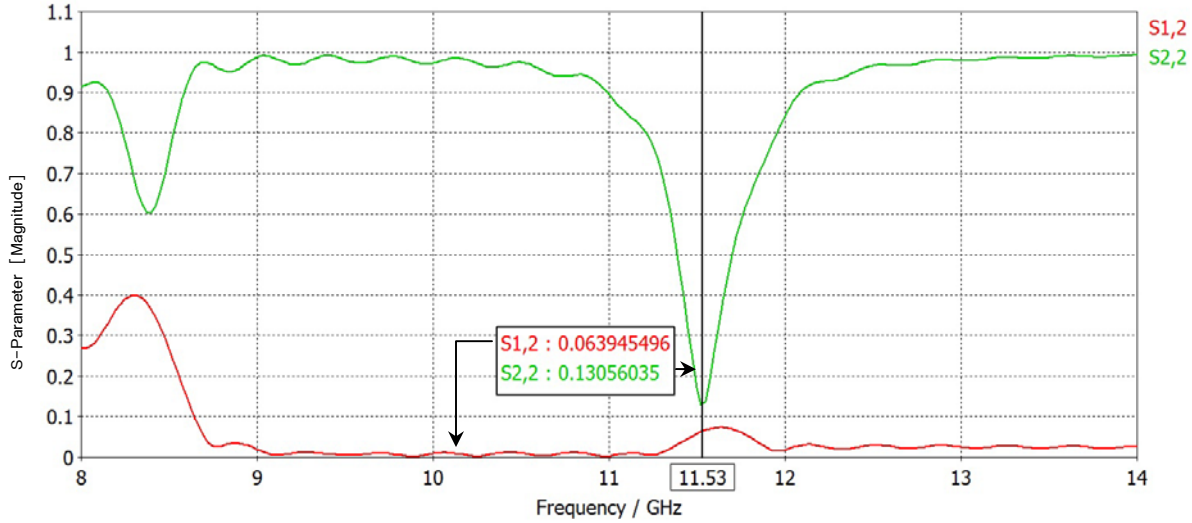

Figure 31. Simulated S-parameters when the conductor thickness is increased to 0.05 mm.

7. Center Conductor

The results in Figures 32–34 are based on the original design in [22] but with a change in the length of the center conductor. The center conductor length was increased beyond the initial design. With a 1-mm extension of the center conductor, the null of S_{22} is deeper (see Figure 33) as compared to the initial design (shown in Figure 32). With a 2-mm extension, the result was like the initial design, but with a shift of frequency. Hence, the design of a 1-mm extension of the center conductor was selected.

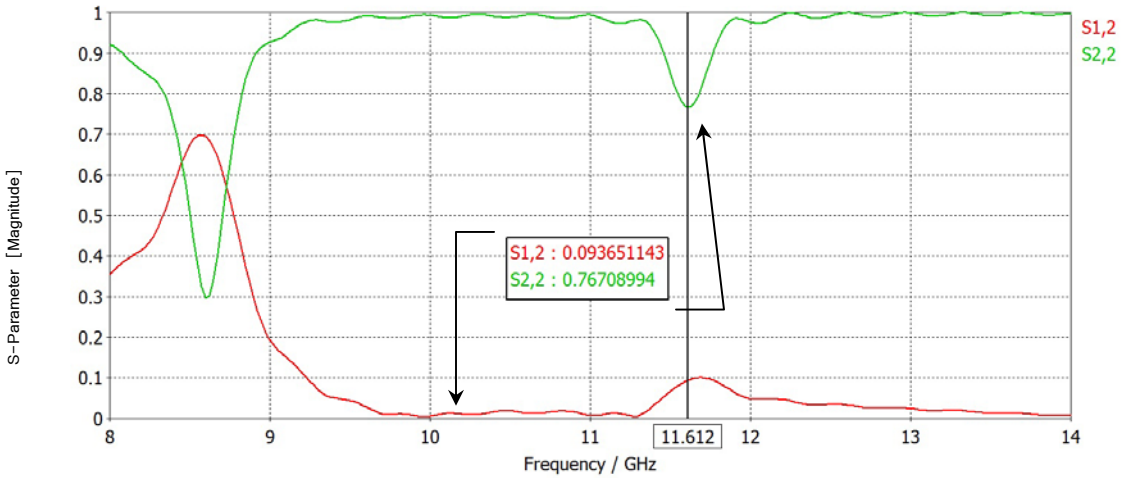

Figure 32. Simulated S-parameters per design in [22].

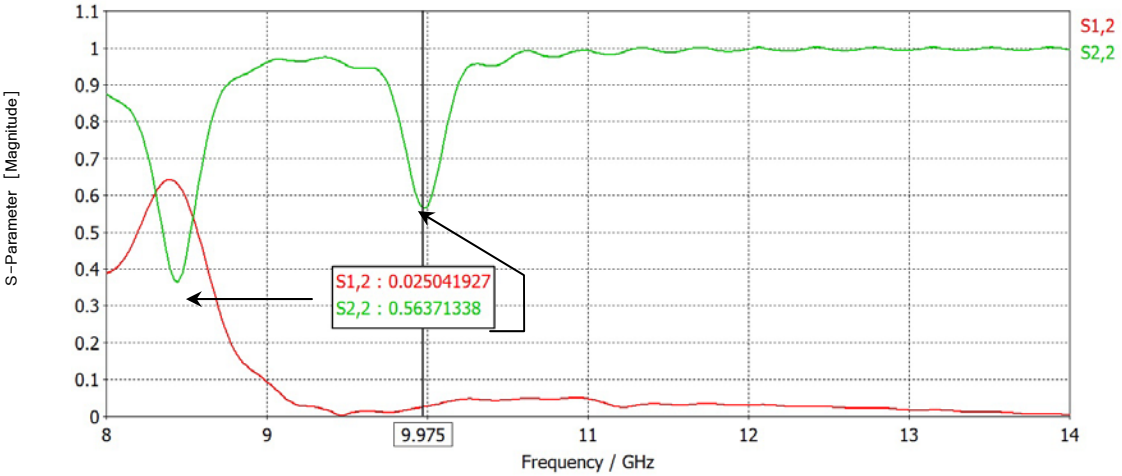

Figure 33. Simulated S-parameters per design in [22], but with center conductor extension of 1 mm.

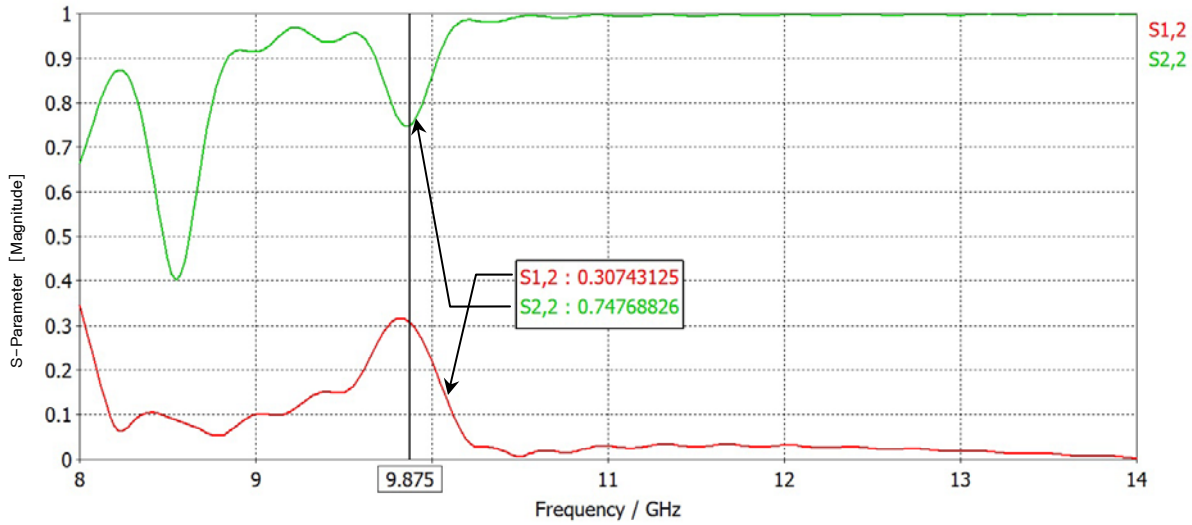

Figure 34. Simulated S-parameters per design in [22], but with center conductor extending 2 mm.

8. Gap

The capacitance between the ends of the upper C and lower C in the design also plays a part in optimizing the result. The null of S_{22} shifts to a higher frequency as the gap increases. From Figures 35–37, it can be seen that a 0.606 mm gap gives the best result.

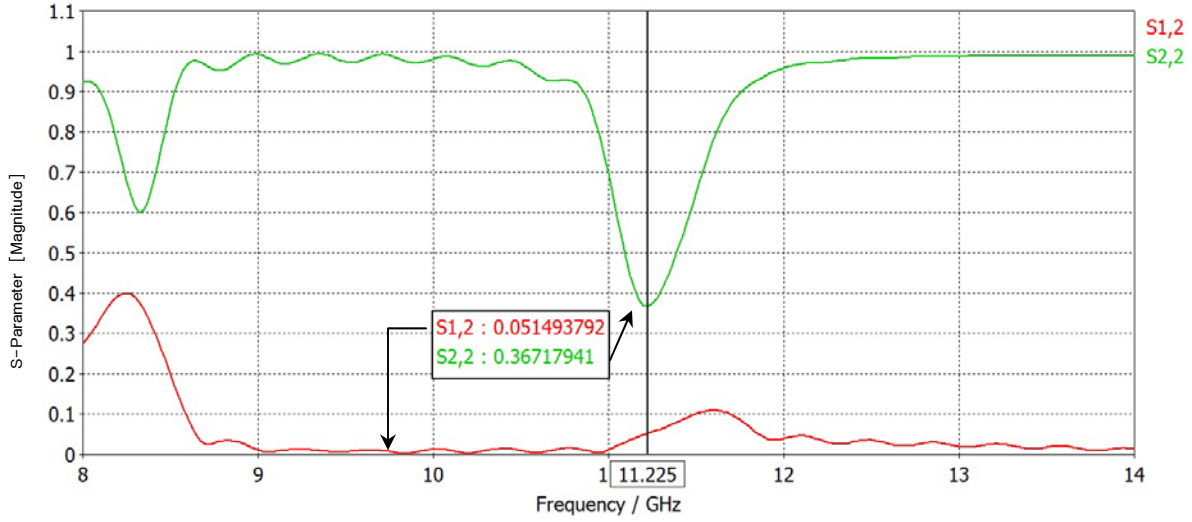

Figure 35. Simulated S-parameters for a gap of 0.3 mm in the design.

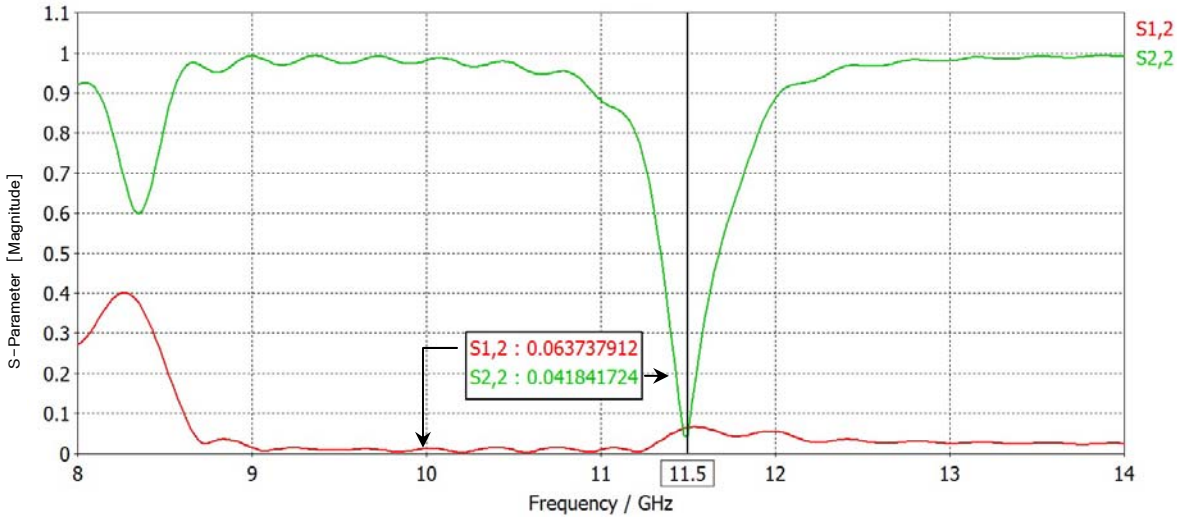

Figure 36. Simulated S-parameters for a gap of 0.606 mm in the design.

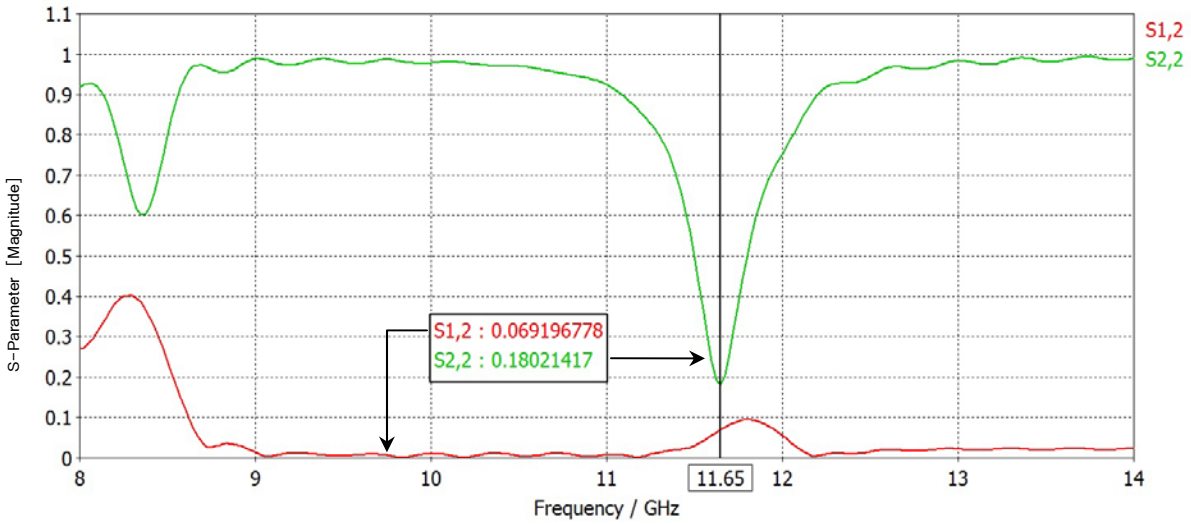

Figure 37. Simulated S-parameters for a gap of 1.0 mm in the design.

9. Overall Performance

The width of the design was the only parameter that was not changed because this dimension was targeted to work at the desired frequency band (X-band), 8–12 GHz. The performance of Design (c) was impressive for normal incident angle, with results for S_{22} of 0.0418 (–27.57 dB) and S_{12} of 0.0637 (–23.91 dB). In reality, most of the time EM

waves do not impinge on the MTM at a normal incidence angles. Therefore, other incident angles are also simulated. The performance for different θ and ϕ angles is tabulated in Table 4 (linear). The Floquet modal analysis option in MWS was used to obtain the data. A standard spherical polar coordinate system is used, as shown in Figure 38.

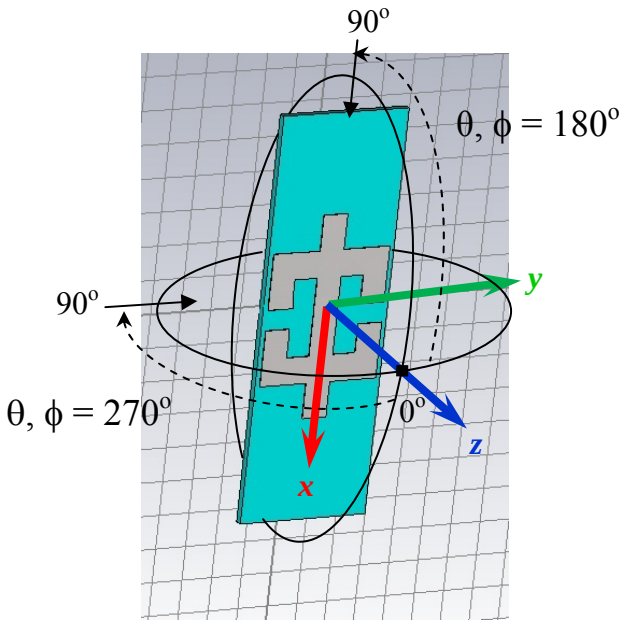

Figure 38. Coordinate system definition for non-normal incidence angles.

Design (c) is symmetrical in the *x* and *y*-planes; therefore, only one quadrant of the results is simulated. Pattern results are as shown in Table 4 and Figures 39 to 41. From the results, we can see that there is good absorption ± 20° from normal incidence less than a 0.178 (–15 dB) change. For the θ angles, there is less than 0.32 (–10 dB) change when $\phi = 0°$, as shown in Figure 39. The results show that absorption decreases as ϕ increases, regardless of θ. The design had very little absorption for large ϕ, as evident in Figures 40 and 41.

When Design (c) was simulated with one port and a metallic backing, the result, as shown in Figure 42, is similarly good, achieving reflectivity S_{11} of 0.02053 (–33.75 dB) at a normal incidence angle. This is the usual material configuration when the design

is applied onto the surface of a platform. In the simulation, the metallic backing is at a distance of 0.85 mm from the last unit-cell, and the reference plane is 0.5 mm in front of the unit-cell facing the port.

The reference plane affects the level of the null but not the bandwidth or frequency of absorption. If the reference plane were closer to the unit cell, the null would be less by a few more decibels. The distance of the reference plane from the port affects the phase of S_{11} and S_{12}. This can also add or subtract a few decibels from the result. This is due to the evanescent modes closer to the structure.

Table 4. Magnitude of reflected EM wave for oblique incidence on Design (c).

Magnitude of reflected EM wave		**Theta (deg)**								
		0	**10**	**20**	**30**	**40**	**50**	**60**	**70**	**80**
Phi (deg)	**0**	0.047	0.059	0.162	0.187	0.229	0.227	0.283	0.324	0.451
	10	0.064	0.065							
	20	0.069		0.090						
	30	0.193			0.310					
	40	0.376				0.546				
	50	0.541					0.672			
	60	0.723						0.755		
	70	0.855							0.755	
	80	0.943								0.944
	90	0.974	0.974	0.973	0.968	0.958	0.938	0.899	0.909	0.957

$\phi = 0^o$ Graph in Figure 39. $\theta = 0^o$ Graph in Figure 40.

$\phi = \theta$ Graph in Figure 41.

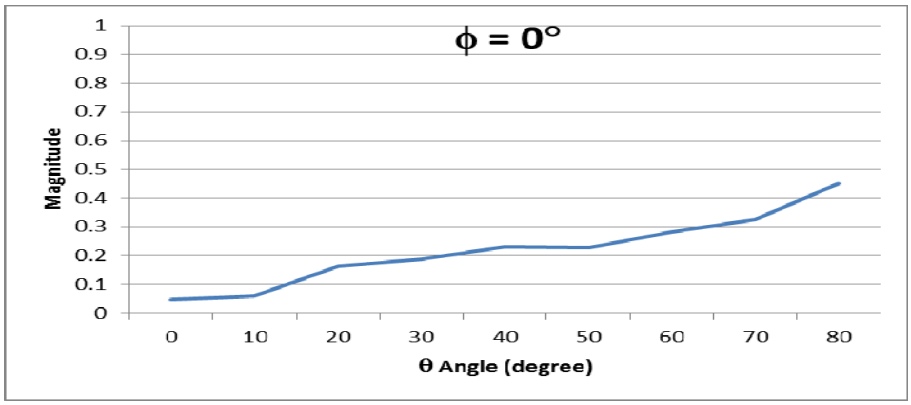

Figure 39. Magnitude of S_{11} at different θ with $\phi = 0^o$.

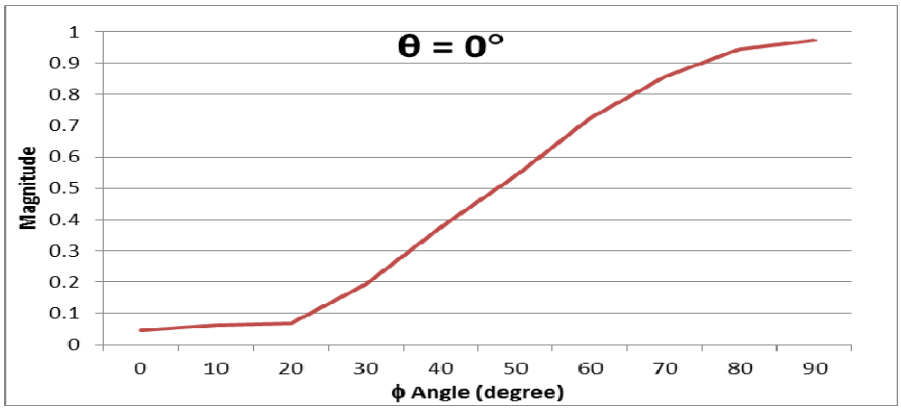

Figure 40. Magnitude of S_{11} at different ϕ with $\theta = 0^o$.

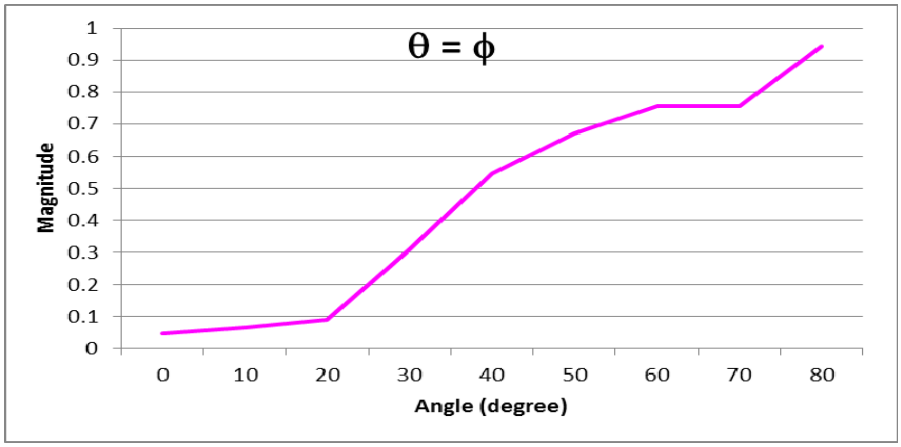

Figure 41. Magnitude of S_{11} when θ equals ϕ.

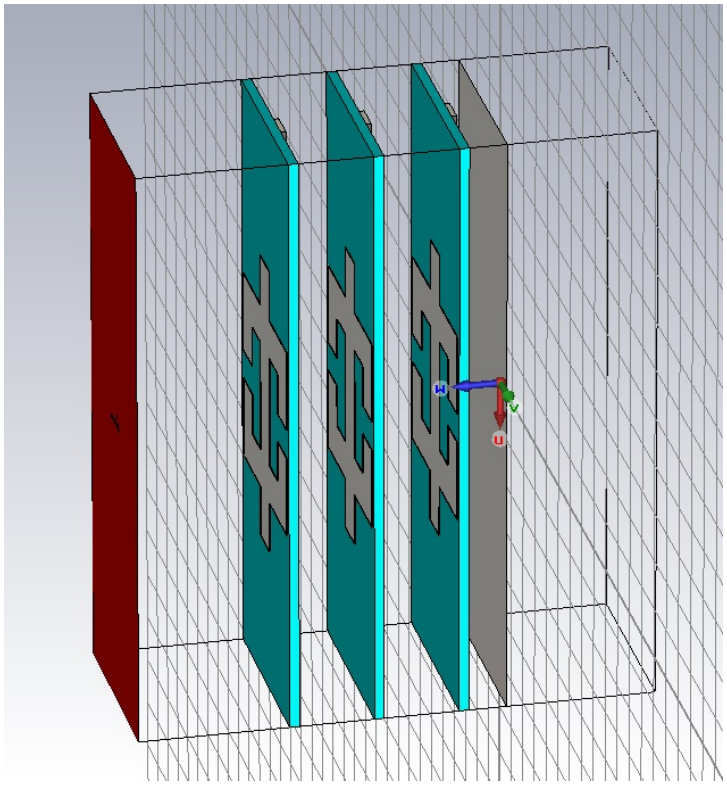

(a)

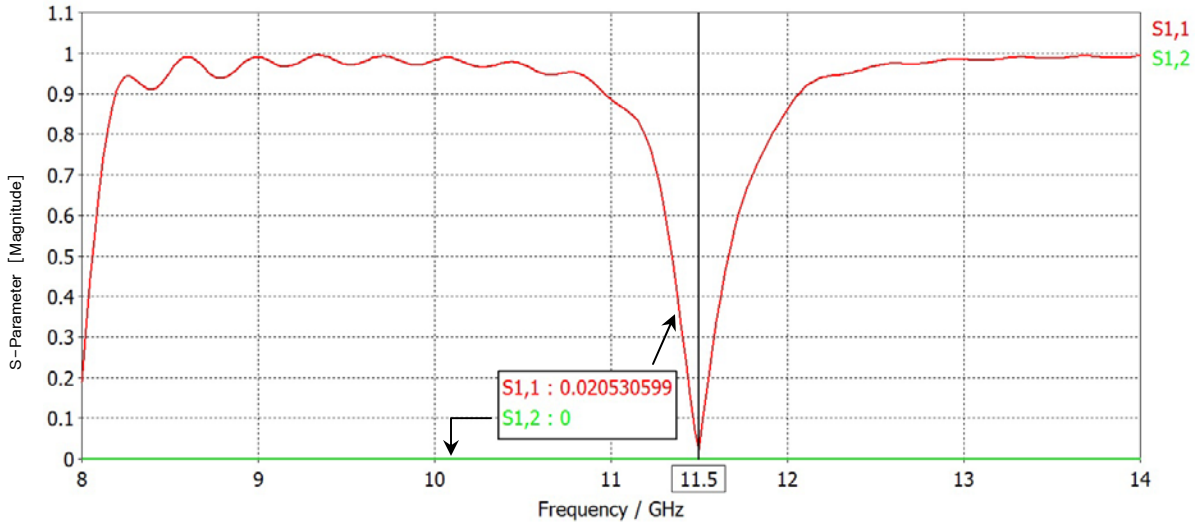

(b)

Figure 42. (a) Design (c) with metallic backing, a configuration likely during application on a platform. (b) Result from this configuration. S_{11} has a value equivalent to a reduction of 33.75 dB. S_{12} is zero, due to the metallic backing, no transmission through a metallic surface.

B. DESIGN (E)

Design (e) was conceived in the process of searching for better results than Design (c). A strip of conductor between the upper and bottom "Cs" was added as a way to increase capacitance. The width of this strip is also *t*, and the gap between this strip and the upper and bottom "C" is still *G*.

Promising results were obtained with initial simulations. Due to time constraints, detailed simulations to explore the full performance of Design (e) were not done. The result for the S_{11} and S_{21} parameters are shown in Figure 43. The null of this design is at 9.0 GHz.

The parameters used in the simulation of Design (e) are shown in Table 5.

Table 5. Parameters used in the simulation of Design (e).

Parameter	**Dimension (mm)**
a_1	4.2
a_2	12.0
W	3.9
G	0.606
t	0.9
L	0.9
H	11.8
Conductor thickness	0.017
Center Conductor Length	8.0
Substrate thickness	0.2
Wire thickness	0.15
Separation distance between unit cell	1.7
Number of unit cell layers	3 pieces

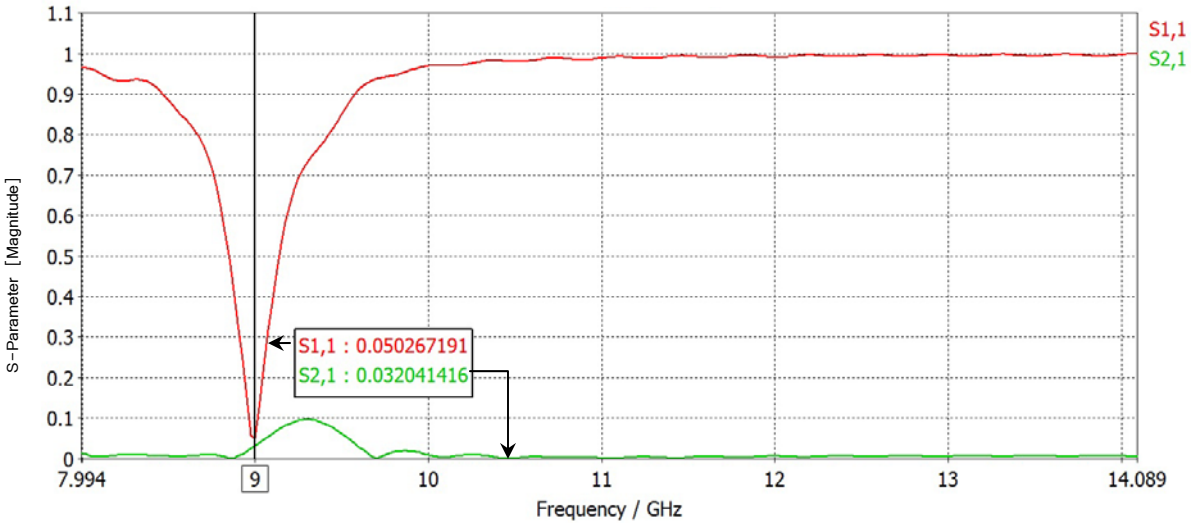

Figure 43. Simulated S-parameters for S_{11} and S_{21} of Design (e).

C. SUMMARY

In this chapter, the design parameters were changed to find the optimal dimensions for each parameter. The dimensions of Design (c) are given in Table 3. The overall performance of Design (c) was evaluated at different incident angles. The results show that Design (c) works well for $\pm 20^{o}$ from the normal, yielding 15 dB of reduction, or more.

The width of the wire, thickness of the wire, separation distance between unit cells, conductor width, and center conductor length significantly affect the frequency where absorption occurs. To design a MTM for a specific frequency, we determined the frequency of choice and tuned the various parameters to make the reflectivity as low as possible. If absorption for another frequency band is required, the size of the whole design must be scaled accordingly; generally, larger for lower frequency bands and smaller for higher frequency bands.

THIS PAGE INTENTIONALLY LEFT BLANK

V. RECOMMENDATIONS AND CONCLUSION

In this chapter, a summary of the research and results for the final design are presented. This chapter concludes with recommendations for future research in the area of MTMs for radar frequencies.

A. SUMMARY AND CONCLUSIONS

The objective of this study was to find a new MTM design for X-band radar frequencies that could be applied to a metallic surface. Hence, this thesis described the design, modeling and simulation of a new MTM, which is a modification of the design in [22]. A detailed description of Design (c) was given, with dimensions in Table 3, so that future researchers will be able to replicate the results and continue the study.

In the optimization of the different parameters of the new design, it was noticed that the absorption frequency is determined by many parameters but mainly by the dimensions of the cell because the dimension W is proportional to the wavelength and determines which band the absorption lies in. Other parameters, like width of wire, thickness of wire, separation distance between unit cells, conductor width, and center conductor, can also affect the absorption frequency, but these parameters are used to fine tune the frequency of absorption and the absorption level.

It has been shown that high absorption can be achieved at normal incidence. The optimal values for the important design parameters have been presented, with a look into how each particular parameter value was chosen. The overall result obtained for Design (c) was 0.0418 (–27.57 dB) for S_{22}, together with a low value of 0.0637 (–23.91 dB) for S_{12}. This design was also simulated with a metallic backing, as would be present in an actual application onto a platform. The S_{11} result achieved for normal incidence is 0.02053 (–33.75 dB).

In the course of this study, questions were raised that could not be addressed due to time constraints. These questions are detailed below for future investigation. It was shown with Design (e) that better performance in some areas is possible.

B. RECOMMENDATION FOR FUTURE STUDIES

Through the course of this research, several issues were raised as to how the performance of the final design can be improved and made applicable to a platform. These questions are described, future studies and possible solutions are recommended in the following subsections.

1. EM Transparent Material Between Unit Cells

Simulations for Design (c) were conducted with a vacuum between the unit cell layers. In the actual fabrication of the structure, the space between the unit cells will be filled by support material. A low dielectric foam can be used without having any impact on the performance. Other possible materials are a thin silicon or polyurethane layer. The permittivity and permeability of these materials will significantly affect the performance, so the layers will have to be included in the MWS simulation to get a more realistic design. A possible implementation using spacers is shown in Figure 44.

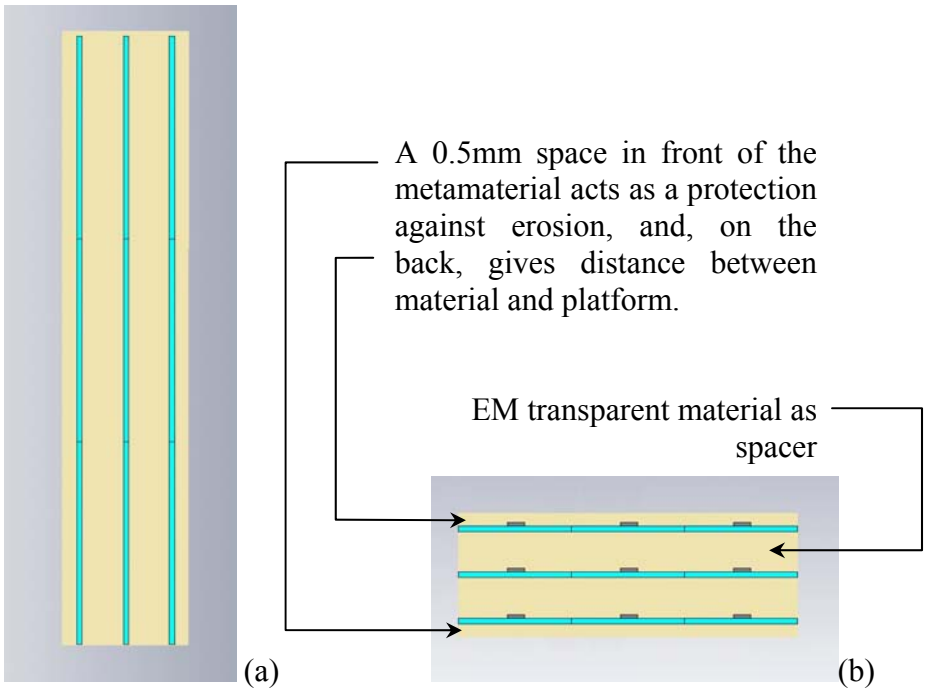

Figure 44. (a) Side view of material. (b) Plan view of material. Design (c) incorporated with EM transparent material spacer. (a) and (b) simulate a large sheet of the metamaterial with Design (c) cascaded horizontally and vertically.

2. Dual-Polarization Design

Design (c) is strictly for vertical polarization; the design works only when the incident wave is vertically polarized. For horizontal polarization, the design does not give any absorption at all. Application for a single-polarization absorber is limited, so modification of Design (c) to handle both horizontal and vertical polarizations should be looked into. References [26] and [27] suggest designs for dual polarization. Some possible designs are shown in Figure 45.

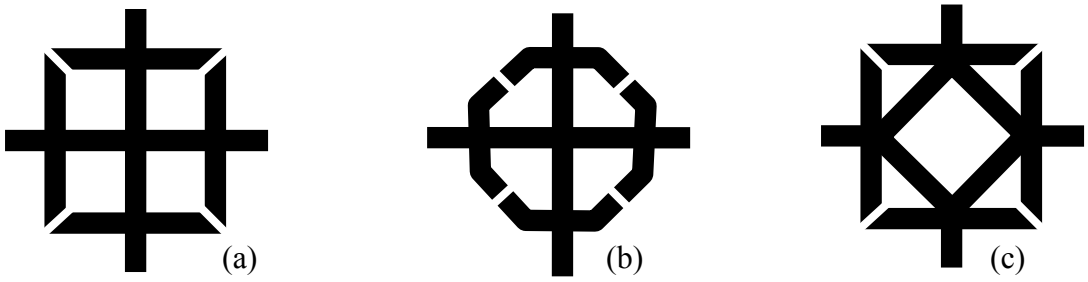

Figure 45. Possible designs for dual polarization.

3. Wideband Absorption

A wideband absorber is favorable since it covers more radar frequencies. Design (c) has absorption of almost 30 dB at 11.5 GHz (dual port measurement), but it is a narrowband absorber with a 10 dB bandwidth of 191 MHz. Most radars hop their frequency to prevent being jammed; therefore, a wider bandwidth of absorption is necessary to truly defeat a radar's detection. An example of a wideband absorber, even though the average absorption level is only 10 dB is given in [26].

4. Circuit Equivalent of Design (c)

Future work to verify the results of Design (c) would be to develop a circuit equivalent. Simulations can be done in Agilent Advance Design System (ADS). A good start is given in [28]. A possible circuit equivalent to Design (c) is shown in Figure 46.

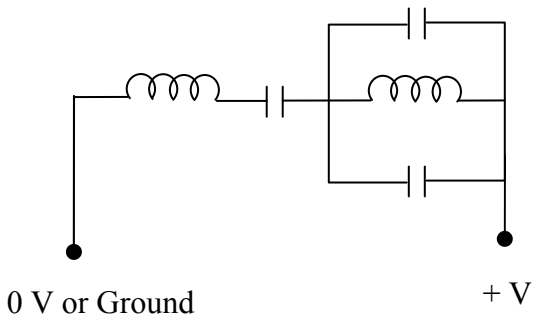

Figure 46. A possible circuit-equivalent model to Design (c).

5. Extracting ε and μ from Scattering Parameters S_{11} and S_{12}

From the results of the simulation it is possible to extract the effective permittivity and permeability from the complex S_{11} and S_{12} data. Using the extracted permittivity and permeability, we can define and simulate a block of material with these properties as bulk material. Both simulations should give the same result. A Matlab code to extract the permittivity and permeability must be written for this application.

LIST OF REFERENCES

[1] http://www.aewa.org/Library/rf_bands.html (Accessed: 8/16/12).

[2] A. Noor, Z. Hu, "Cloaking of metallic sub-wavelength objects by plasmonic metamaterial shell in quasistatic limit," *IET Microwaves, Antennas & Propagation*, vol 3, no.1, pp. 40–46, 2009.

[3] Yan Liu, Xiao Wei, HuanQing Wang, ZhuZhen Li, HongCheng Yin, PeiKang Huang, "Backscattering of metamaterial electromagnetic cloak," *2008 International Workshop on Metamaterials*, pp. 335–337, 2008.

[4] Fei Ding, Yanxia Cui, Xiaochen Ge, Yi Jin, and Sailing He, "Ultra-broadband microwave metamaterial absorber," *Appl. Phys. Lett.* vol. 100, paper 103506, 2012.

[5] V.G. Veselago, "The electrodynamic properties of a mixture of electric and magnetic charges," *Soviet Physics Journal of Experimental and Theoretical Physics*, vol. 25, pp. 680,1967.

[6] Lee, H.S., Park, J.W., Lee, H.M., "Design of double negative metamaterial absorber cells using electromagnetic-field coupled resonators," *Microwave Conference Proceedings (APMC), 2011 Asia-Pacific,* pp. 1062–1065, 2011.

[7] Varadan, V.V., "Radar Absorbing Applications of Metamaterials," *Region 5 Technical Conference, 2007 IEEE,* Digital Object Identifier: 10.1109/TPSD.2007.4380361, pp. 105–108, 2007.

[8] V. G. Veselago, "The electrodynamics of substances with simultaneously negative values of ε and μ," *Sov. Phys. Uspekhi* , vol. 10, no. 4, pp. 509–514, 1968. [*Usp. Fiz.Nauk*, vol. 92, pp. 517–526, 1967].

[9] J. B. Pendry, A. J. Holden, W. J. Stewart and I. Youngs, "Extremely Low Frequency Plasmons in Metallic Mesostrucrures," *Phy. Rev. Letters,* vol 76, no, 25, pp. 4773–4776, 1996.

[10] R. A. Shelby, D. R. Smith, S. C. Nemat-Nasser and S. Schultz, "Microwave transmission through a two-dimensional, isotropic, left-handed metamaterial," *Appl. Phys. Lett.*, vol 78, no. 4, pp. 489, 2001.

[11] Ilya Shadrivov and Yuri Kivshar, "Bending waves in a wrong way," *The Pyhsicist*, vol 41, no. 4, pp. 137, 2004.

[12] Atsushi Sanada, Christophe Carloz and Tatsuo Itoh, "Planar distributed structures with negative refractive index," *IEEE Trans. on Microwave theory and techniques*, vol 52, no. 4, pp.1252–1263, 4 April 2004.

[13] Peter Markos and C.M. Soukoulis, "Transmission properties and effective electromagnetic parameters of double negative metamaterials," *Optics express*, vol.11, no. 7, pp. 649–661, 7 April 2003.

[14] R. Gómez Martín, *Electromagnetic field theory for physicists and engineers: Fundamentals and Applications*, Granada, pp. 21, Físicas Curso 2006–2007.

[15] D. C. Jenn, Notes for EC3630 (Radiowave Propagation), Naval Postgraduate School, 2003 (unpublished).

[16] Nader Engheta and Richard W. Ziolkowski, "A positive future for double-negative metamaterials," *IEEE Trans. Microwave Theory Tech.*, vol 53, no. 4, 2005.

[17] Bo-Kai, Feng, "Extracting material constitutive parameters from scattering parameters," Naval Postgraduate School Thesis, Sep. 2006.

[18] X.Chen, T. M. Grzegorczyk, B. I. Wu, J. Pacheco Jr., and J. A. Kong, "Robust Method to Retrieve the Constitutive Effective Parameters of Metamaterials," *Phys. Rev. E*, vol. 70, paper 016608, 2004.

[19] Nader Engheta and Richard W. Ziolkowski, "Introduction, history, and selected topics in fundamental theories of metamaterials," in *Metamaterials : Physics and Engineering Explorations,* pp. 17–19, IEEE Explore Digital Library (2010), (Books - Metamaterials section). Retrieved 2010-05-01., John Wiley & Sons, Inc., 2006.

[20] J. B. Pendry, A. J. Holden, D. J. Robbins, and W. J. Stewart, "Magnetism from Conductors and Enhanced Nonlinear Phenomena," *IEEE Trans. Microwave Theory Tech.*, vol 47, no.11, pp. 2075–2084, November 1999.

[21] Computer Simulation Technology, *CST Microwave Studio – Getting Started*, Computer Simulation Technology, Darmstadt (Germany), pp. 4–6, 2005.

[22] N. I. Landy, S. Sajuyigbe, J. J. Mock, D. R. Smith, and W. J. Padilla, "Perfect Metamaterial Absorber," *Phys. Rev. Letters*, vol. 100, paper 207402, 2008.

[23] W. J. Padilla, M. T. Aronsson, C. Highstrete and Mark Lee, A. J. Taylor and R. D. Averitt, "Electrically resonant terahertz metamaterials: Theoretical and experimental investigations," *Phy. Rev. B*, vol 75, paper 041102 (R), 2007.

[24] D. R. Smith, D. C. Vier, Willie Padilla, Syrus C. Nemat-Nasser, and S. Schultz, "Loop-wire medium for investigating plasmons at microwave frequencies," *Applied Physics Letters*, vol 75, no. 10, pp. 1425, 1999.

[25] http://www.cst.com/Content/Applications/Article/Article.aspx?id=355 (Access : 8/1/2012).

[26] A. Noor, Z. Hu, "Metamaterial dual polarised resistive Hilbert curve array radar absorber," *IET Microwaves, Antennas & Propagation*, vol 4, no.6, pp. 667–673, 2010.

[27] Youngsoo Jang, Joungyoung Lee, Sungjoon Lim, "Incident Angle Insensitive Double Negative (DNG) Metamaterial Absorber," *Microwave Conference Proceedings (APMC), 2011 Asia-Pacific,* pp. 1870–1872, 2011.

[28] Wakatsuchi, H., Paul, J., Greedy, S., Christopoulos, C., "Cut-Wire Metamaterial Design Based on Simplified Equivalent Circuit Models," *IEEE Trans. on Antennas and Propagation, v*ol 60 , no. 8, pp. 3670–3678, 2012.

THIS PAGE INTENTIONALLY LEFT BLANK

INITIAL DISTRIBUTION LIST

1. Defense Technical Information Center
   Ft. Belvoir, Virginia

2. Dudley Knox Library
   Naval Postgraduate School
   Monterey, California

3. Professor R. Clark Robertson
   Chairman, Department of Electrical and Computer Engineering
   Naval Postgraduate School
   Monterey, California

4. Professor David C. Jenn
   Department of Electrical and Computer Engineering
   Naval Postgraduate School
   Monterey, California

5. Dr James Calusdian
   Department of Electrical and Computer Engineering
   Naval Postgraduate School
   Monterey, California

6. Professor Yeo Tat Soon
   Director, Temasek Defence System Institute (TDSI)
   National University of Singapore
   Singapore, Singapore

7. Ms Tan Lai Poh
   Senior Manager, Temasek Defence System Institute (TDSI)
   National University of Singapore
   Singapore, Singapore

8. Mr Fong Saik Hay
   CTO, ST Engrg,
   ST Engineering
   Singapore, Singapore

9. Mr R. Balakrishnan
   Vice President, VTE
   Singapore Technologies Aerospace Limited
   Singapore, Singapore